JOURNAL OF MAGNETIC RESONANCE IMAGING 37:1301–1325 (2013)

Review

MR Spectroscopic Imaging: Principles and Recent Advances

Stefan Posse, PhD,[1–3]* Ricardo Otazo, PhD,[4] Stephen R. Dager, MD,[5] and Jeffry Alger, PhD[6]

MR spectroscopic imaging (MRSI) has become a valuable tool for quantifying metabolic abnormalities in human brain, prostate, breast and other organs. It is used in routine clinical imaging, particularly for cancer assessment, and in clinical research applications. This article describes basic principles of commonly used MRSI data acquisition and analysis methods and their impact on clinical applications. It also highlights technical advances, such as parallel imaging and newer high-speed MRSI approaches that are becoming viable alternatives to conventional MRSI methods. Although the main focus is on ^{1}H-MRSI, the principles described are applicable to other MR-compatible nuclei. This review of the state-of-the-art in MRSI methodology provides a framework for critically assessing the clinical utility of MRSI and for defining future technical development that is expected to lead to increased clinical use of MRSI. Future technical development will likely focus on ultra-high field MRI scanners, novel hyperpolarized contrast agents using metabolically active compounds, and ultra-fast MRSI techniques because these technologies offer unprecedented sensitivity and specificity for probing tissue metabolic status and dynamics.

Key Words: MR spectroscopic imaging; chemical shift imaging; spatial and spectral encoding; spatial prelocalization; spectral quantification; echo-planar spectroscopic imaging; parallel imaging; compressed sensing; human; brain; breast

J. Magn. Reson. Imaging 2013;37:1301–1325.

MR SPECTROSCOPIC IMAGING (MRSI) is a widely available routine clinical imaging tool and clinical research tool for spatially mapping multiple tissue metabolites signals in vivo to characterize neurological, psychiatric and metabolic disease. This technology, which is available on many clinical MR scanners, has reached a remarkable degree of maturity in recent years and has stimulated considerable interest in clinical applications. The purpose of this article is to introduce the technological features of MRSI in a manner that can be readily understood and appreciated by the practicing radiologist who is not a physicist or MRS specialist. As most MRSI development and applications have been focused on the brain, MRSI (as well as MRS in general) is sometimes viewed as having importance only within the neuroradiological community. This article includes the description of MRSI applications that extend beyond the field of neuroradiology. Accordingly, the article is formulated with the general radiologist in mind and will introduce and explain key MR physics/technology concepts with this target audience in mind. It will also summarize key literature both in terms of physics concepts and the practical realization of these concepts for the clinical radiological examination.

A variety of synonymous terms for MRSI, including Chemical Shift Imaging (CSI), Spectroscopic Imaging (SI) and Multivoxel Spectroscopy (or Multivoxel MRS), have been used in the literature and by scanner vendors. This article will use a single term (MRSI) to denote all of these. To a large extent, MRSI technology is built upon earlier work developing localized single voxel MRS (SV-MRS). First described by Brown et al in 1982 (1) and further developed by Maudsley et al in 1983 (2), MRSI increasingly is supplanting SV-MRS for clinical applications and research due to its ability to rapidly and simultaneously assess tissue spatial heterogeneity of chemical concentrations. However, several technical challenges currently limit more

[1]Department of Neurology, University of New Mexico School of Medicine, Albuquerque, New Mexico, USA.
[2]Department of Electrical and Computer Engineering, University of New Mexico, Albuquerque, New Mexico, USA.
[3]Department of Physics and Astronomy, University of New Mexico, Albuquerque, New Mexico, USA.
[4]Bernard and Irene Schwartz Center for Biomedical Imaging, New York University School of Medicine, New York, New York, USA.
[5]Department of Radiology, University of Washington School of Medicine, Seattle, Washington, USA.
[6]Department of Neurology, Department of Radiological Sciences, Interdepartmental Program in Biomedical Engineering, David Geffen School of Medicine at UCLA, University of California, Los Angeles, California, USA.

Contract grant sponsor: NIH; Contract grant number: 1 R01 DA14178-01, RO1 EB00822, R01 MH081864, RC1 MH088507, RO1 NS036524, ARRA-1R01HD065283, 1P50 HD055782; Contract grant sponsor: the MIND Research Network (DOE Grant); Contract grant number: DE-FG02-99ER62764; Contract grant sponsor: the University of New Mexico School of Medicine Brain and Behavioral Illness Signature Program.

*Address reprint requests to: S.P., Department of Neurology, The University of New Mexico School of Medicine, 1 University of New Mexico, MSC 105620, Albuquerque, NM. E-mail: sposse@unm.edu

Received January 24, 2012; Accepted October 11, 2012.
DOI 10.1002/jmri.23945
View this article online at wileyonlinelibrary.com.

widespread clinical acceptance of MRSI. Furthermore, MRSI historically has required a high degree of user training and integration into clinical routine is nontrivial. This article is specifically focused on MRSI technology. It does not summarize either the background physics or use of localized SV-MRS except where there are important shared features or noteworthy differences. It assumes that the reader is familiar with basic MRS concepts, such as chemical shift, J-coupling and multiplet spectral patterns. It is also not feasible to present a detailed review of the biological or clinical relevance of the detectable metabolite signals that can be quantitatively mapped by MRSI, and which has been extensively reviewed elsewhere (3). In addition to presenting basic principles, this article highlights recent advances such as high-speed MRSI methods and MRSI with parallel receiver array coils, which are becoming increasingly relevant for clinical research applications. The main focus is on brain proton (^{1}H)-MRSI, which is well established, but the methods are applicable for other MR-compatible nuclei and tissue types and recent examples of these applications are also presented.

GENERAL FEATURES OF MRSI

In general terms, MRSI uses the same phase encoding procedures that are used in MRI to map the spatial distribution of MR signals. In the case of ^{1}H-MRSI, proton MR signals produced by metabolites within the tissue produce the signals that are imaged. The molecular concentrations of these metabolites are at least 10,000 times lower than water and metabolites produce correspondingly much lower signal strengths than does water, which is used to form conventional MR images. To detect enough signal above noise for quantification ^{1}H-MRSI must use much larger voxel sizes in comparison to MRI. Voxel volumes on the order of 0.3 cc can be readily measured at 3T (4,5) and the use of surface coils and array coils allows much smaller voxel volumes on the order of 0.1 cc (6), or smaller. The lower spatial resolution of MRSI compared with anatomical imaging makes consideration of the spatial point spread function (PSF), correspondingly more important. The PSF expresses the fact that the combination of the phase-encoded imaging process and the image reconstruction process cause metabolite signals that are produced by one tissue voxel to bleed into the surrounding voxels, producing a blurring effect. This is conceptually not different from conventional MRI, but is expressed on a larger spatial scale. The PSF can be responsible for spectral artifacts and significant partial volume effects. Spatial filtering is used in the reconstruction process to reduce between-voxel signal bleeding and to increase the signal-to-noise ratio (SNR), but increases the effective voxel size. MRSI can be time consuming to acquire, making it sensitive to motion artifacts, which in contrast to MRI are distributed across all acquired spatial dimensions.

MRSI is also highly sensitive to macroscopic magnetic field inhomogeneity within a voxel and across the volume of interest, which introduces regionally varying spectral line broadening. Typically, a spectral line width of less than 0.1 part per million (ppm) is required for quantifiable MRSI data. Accordingly, MRSI studies may require sacrificing coverage of some anatomical regions having strong magnetic field inhomogeneity. Unacceptable field homogeneity is usually present at tissue-bone or tissue-air interfaces and such regions are difficult to study with MRSI. In these regions SV-MRS may be the only choice.

In ^{1}H-MRSI there are often artifacts related to water and lipid signals that are related to field inhomogeneity and the PSF. Water produces a much larger signal than the target metabolites. ^{1}H-MRSI pulse sequences use frequency selective RF pulses to presaturate the water signal, but magnetic field homogeneity associated with interfaces can produce water signal that is frequency shifted and the water suppression process will not suppress water signal being produced by interface regions. Furthermore, water signal produced by such regions is broadened as well, which makes signal contamination due to the blurring effect difficult to identify. Lipid signals that are as much as 1000 times stronger than metabolite signals can be produced by tissues that have a large fraction of adipocytes. Lipid signals produced by such regions can also be problematic in terms of bleeding into nearby voxels. Because the problem of lipid and water signal bleeding can be so significant in ^{1}H-MRSI, very precise spatial localization methods are required. Most ^{1}H-MRSI pulse sequences use volume excitation procedures analogous to those used in SV-MRI to select a box shaped tissue region over which the field homogeneity is excellent and that does not contain adipose tissue. Alternatives are to presaturate regions that would produce large lipid signal or have unacceptable field homogeneity, or to use lipid nulling using the Short T_1 Inversion Recovery (STIR) (7). While improving overall results quality, prelocalization of a box-shaped region inside the organ of interest can result in considerable loss of volume coverage in peripheral regions of the organ.

Furthermore, the majority of ^{1}H-MRSI studies to date are still performed using intermediate to long echo time (TE) to attenuate lipid signals due to short lipid signal T_2 values. This is in part due to the difficulties of quantifying strongly overlapping multiplet resonances at short TE. However, the use of long TE results in substantially decreased sensitivity to the metabolite signals due to T_2 loss and J-modulation of multiplet resonances. Improved localization performance now allows MRSI mapping at much shorter TE, to measure J-coupled metabolites that have traditionally been measurable only with SV-MRS (8).

MRSI studies that involve nuclei other than protons, usually do not have problems corresponding to the lipid and water problems present in ^{1}H-MRSI, but signal strength in these studies is usually lower than in ^{1}H-MRSI and the volume resolution must be even more coarse and this engenders more concern regarding voxel signal bleeding.

SPECTROSCOPIC IMAGING ACQUISITION AND RECONSTRUCTION

Conventional phase-encoded MRSI, in which the phase encoding gradient amplitude is incremented

once per TR, is the most commonly used MRSI method and still represents the gold standard for sensitivity and for localization performance. This section provides an overview of conventional phase-encoded and newer high-speed MRSI methods, compares their performance (acceleration, signal-to-noise per unit volume and square root of unit measurement time, spectral width, spectral resolution, and point spread function) and discusses technical challenges at high field strength. A simplified description of methods is presented without the *k*-space formalism to provide an intuitive understanding that is fully adequate for clinical applications. The *k*-space formalism, which provides an overarching framework for linking the different MRSI methodologies, will be added where appropriate to provide a deeper understanding.

Phase-Encoded Spectroscopic Acquisition

As with all MRI methods, MRSI uses a modular pulse sequence design. Frequency encoding of spatial location using gradient application during the signal detection period in the pulse sequence is not used in conventional MRSI, because doing so mixes the spatial and chemical shift information in a manner that is difficult to disentangle. The use of phase encoding only to obtain location information ensures complete temporal separation of spatial encoding from spectral encoding to avoid possible line broadening due to the application of gradients (except for effects from possible eddy currents). Phase encoding merely modulates the signal phase and amplitude of the MR signal before detection of signal frequency (spectral encoding), which ensures that subsequent phase and amplitude modulation due to chemical shift is independent of spatial encoding. Data reconstruction is, therefore, straightforward using Fourier transformations along the orthogonal spatial and spectral dimensions of the raw data matrix. Localization by phase encoding (using constant phase encoding gradient duration) is also unaffected by chemical shift and magnetic field inhomogeneity unlike readout encoding. In other words, image shape distortions due to field inhomogeneity or chemical shift (e.g., fat–water shift) are not present in MRSI.

However, phase encoding must be performed in all spatial dimensions and is very time consuming. The number of phase encoding steps corresponds to the total number of voxels in the spectroscopic image. For example, to acquire a 32 × 32 × 16 three-dimensional (3D) matrix using a TR of 2 s would require 32,768 s, or more than 9 h of encoding time, which is quite unacceptable for human studies. Typical raw data 2D matrix sizes used in clinical research studies are much smaller: 16 × 16, 24 × 24, or 32 × 32 data point points, but still require substantial acquisition time using conventional MRSI.

To gain a deeper understanding of phase encoding, it is instructive to take a closer look at the relationship to readout (frequency) encoding. Readout encoding is a familiar concept that is straightforward to conceive of as a projection image along the direction of the readout gradient that is obtained by Fourier transformation of the acquired signal. The readout signal consists of a series of data points that record stepwise changes of signal phase and amplitude during the application of the readout gradient. Phase encoding can be viewed as being equivalent to acquiring the readout signal on a data point by data point basis from separate measurements. This equivalence is illustrated in Figure 1, which shows the transition from readout to phase encoding. To center the "phase encoding echo" in data space, the phase encoding gradient starts with negative amplitude and steps to positive amplitudes, which is comparable to using a dephasing gradient to center the readout echo in MRI. Indeed, the gradient moment (= amplitude x duration) of the minimum (i.e., most negative) phase encoding gradient corresponds to the moment of the dephasing gradient. The difference between the moments of the maximum and the minimum phase encoding

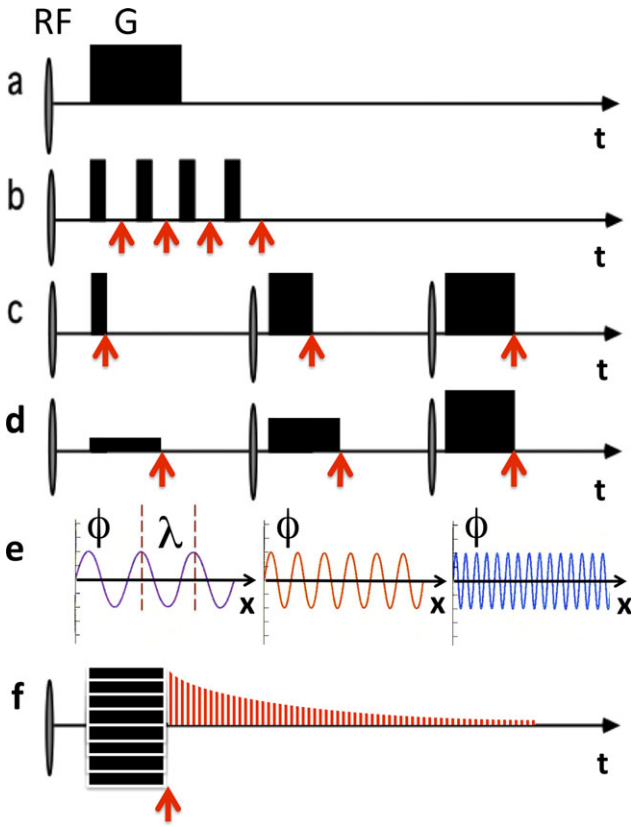

Figure 1. Principles of MRSI. **a–c**: Equivalence of readout and phase encoding illustrated by stepwise transformation of readout encoding into phase encoding. (b) Segmentation of the readout gradient "G" into gradient pulses with interleaved collection of single data points (red arrows). **c**: Collection of the same data points in separate experiments using phase encoding. **d**: Phase encoding with constant gradient duration. **e**: Spatially periodic spin phase distribution along the direction of the phase encoding gradients; the spatial periodicity of the spin phase, which is characterized by the wavelength λ, increases with the stepwise increase in the phase encoding gradient amplitude. **f**: Spectroscopic imaging by combining phase encoding with a spectroscopic readout; the amplitude and phase of the initial data point (red arrow) represents the spatial information embedded in the spectroscopic signal. [Color figure can be viewed in the online issue, which is available at wileyonlinelibrary.com.]

gradients corresponds to the moment of the readout gradient and determines spatial resolution. The increment in gradient moment between phase encoding gradient steps corresponds to the increase in gradient moment between digitization steps of the readout signal and determines the encoded field-of-view (FOV).

K-t-Space in MRSI

The *k*-space formalism is an elegant description of raw data space, which provides a unified framework for the comparison of different spatial encoding methods and which facilitates the analysis of localization properties and artifacts. *K*-space is formed by a set of spatially periodic rotations of the spin phase across the object that is generated in successive experiments by the application of the phase encoding gradients (referred to as spin warp imaging) (9) (Fig. 1e). The periodic spin phase rotations, which are characterized by the wavelength λ, increase with the moment (amplitude G × duration t) of the applied phase encoding gradients and range from infinity (no phase modulation at the center of *k*-space) to very rapid periodicities corresponding to the smallest features that are present in the object. The spatial frequency of the spin periodicities (= 1/λ) is characterized as:

$$k = \frac{2\pi}{\lambda} = \gamma G t \qquad [1]$$

The *k*-space formalism describes the structure of the spatially encoded data in form of a set of spatial frequencies (the inverse of object space), which after Fourier transformation represents the image of the object. Each data point in *k*-space corresponds to the signal from the entire sensitive volume of the receiver coil and represents a unique spatial modulation of the spin phases of the entire object along the directions of the phase encoding gradients. The moment of the phase encoding gradients determines the phase rotation each spin experiences relative to the magnet center. It is this spatial distribution of spin phases generated by the phase encoding gradients that unambiguously identifies each point in the object and allows spatial reconstruction of an image. In MRSI, the time dimension corresponding to spectral encoding is encoded orthogonal to *k*-space to form *k*-t-space, which for 2-dimensional spatial encoding forms a 3-dimensional data space (k_y-k_x-t). Each *k*-t-space slice at a particular time point (a time slice) can be reconstructed into an "image" by Fourier transformation. Fourier transformation along the series of consecutive images generates localized spectra.

The MRSI signal of a chemical species with frequency ω after the application of a phase encoding gradient is defined as:

$$S(k,t) = \int \sigma(x) e^{i\omega t} e^{i2\pi kx} dx \qquad [2]$$

where σ(x) is the spin density of the object along the vector direction x of the applied phase encoding gradients and k is the encoded spatial frequency. The MR signals obtained with different phase encoding steps completely characterize the spin density distribution of the object (a simple analogue is the optical interference pattern of a phonographic record that unambiguously defines the music piece that is encoded in the groves of the record) and the spectral information content.

There are five simple rules that describe *k*-space encoding: (i) The extent of *k*-space determines spatial resolution. (ii) The spacing between successive sampled points (phase encoding increment, or step size) along a given *k*-space direction corresponds to the encoded FOV along the corresponding spatial direction. (iii) Coarse features of the object are encoded close to the center of *k*-space (low spatial frequencies). (iv) Details of the object are encoded at the periphery of *k*-space (high spatial frequencies). (v) *K*-space in a spin echo experiment is (hermitian) symmetric with respect to the center, i.e., data points on opposite sides of the center have identical amplitude, but complex conjugate phase. Encoding the entire *k*-space is thus redundant and partial Fourier encoding might be considered to accelerate encoding, although magnetic field inhomogeneities and other imperfections limit this approach, as we will see below.

PSF and Acceleration of Phase Encoding

Spatial localization in MRSI cannot be characterized without discussing the PSF, which describes the spread of signal from a point source into adjacent voxels as a result of the finite extent of the encoded *k*-space, a direct consequence of the coarse spatial resolution of MRSI. For uniform *k*-space sampling, the PSF is a sinc (= sinx/x) function (the Fourier transform of the boxcar sampling window) with the full width at half maximum being the linear voxel dimension. For a point source in the center of the voxel the zero crossings of the PSF are exactly in the centers of the adjacent voxels, i.e., there is no signal spread to adjacent voxels and the image of the point source is a single bright voxel (Fig. 2a). The situation is very different for a point source located at the edge of a voxel, which leads to considerable spread of signals into adjacent voxels (Fig. 2b). Note that the signal contamination has positive and negative contributions depending on the distance from the origin of the PSF, which can lead to very complex signal interference. For example, in ^{1}H-MRSI the signal spread from a peripheral fat layer in the scalp that is located at the interface of two adjacent voxels can leads to strong baseline distortions in nonadjacent, even central, brain voxels. This so-called Gibbs ringing is also present in conventional MRI, in particular affecting edges with large image contrast, but it is less conspicuous than in MRSI due to the considerably higher spatial resolution. To reduce Gibbs ringing for MRSI it is necessary to apply rather aggressive *k*-space filters in the image reconstruction that suppress the outer regions of *k*-space and correspondingly reduce spatial resolution. Sinebell, Fermi and Hamming filter functions are examples of commonly used *k*-space filters to control spatial signal contamination. For a rectangular *k*-space matrix the extent of *k*-space along the

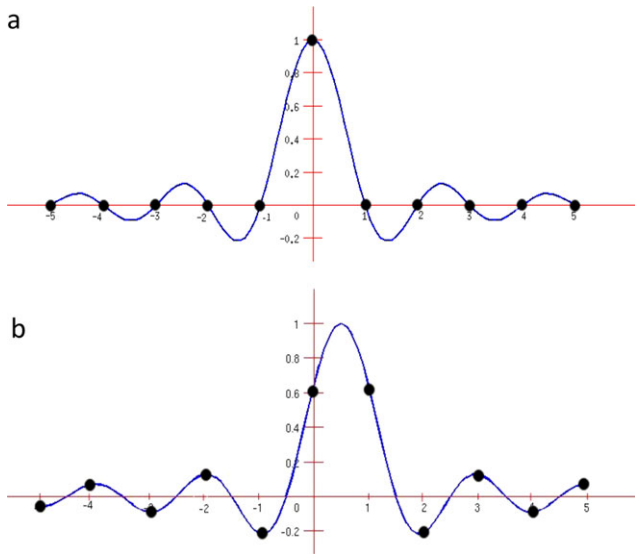

Figure 2. Point spread function in MRSI for (**a**) a point source located in the center of the voxel (x = 0), which results in perfect localization without any signal contamination in adjacent voxels and (**b**) a point source located at the right edge of the voxel (x = 0.5), which results in a significant signal contamination into adjacent voxels. [Color figure can be viewed in the online issue, which is available at wileyonlinelibrary.com.]

diagonals is $\sqrt{2}$ larger than along the principal axes, which results in a narrower point spread function and increased spatial resolution along the diagonals. As a consequence, Gibbs ringing is stronger along the principal axes compared with the diagonals.

A frequently used strategy to accelerate phase-encoded MRSI is to sacrifice the higher spatial resolution along the diagonal and to cut the *k*-space corners to encode a spherical or an elliptical *k*-space, which can reduce measurement time by as much as 50% for 3D encoding. The PSF for elliptical sampling is uniform along all directions, but overall spatial contamination and voxel size are increased compared with rectangular sampling. A further increase in encoding speed can be achieved when signal averaging is necessary for sensitivity reasons. Weighted averaging, in which fewer averages are collected at peripheral *k*-space points compared with central *k*-space points, further reduces scan time, albeit at the expense of having increased high frequency noise relative to low frequency noise in the reconstructed spectroscopic image.

Magnetic Field Inhomogeneity and Effect on k-t-Space Encoding

It is instructive to consider the effects of magnetic field inhomogeneity, shimming and spatial resolution on *k*-t-space encoding to understand the measured signal distribution in the acquired data space. The *k*-space acquired at the center of the spin echo is perfectly (hermitian) symmetric on lines through the origin of *k*-space. In a perfectly shimmed sphere, *k*-space is invariant along the time domain, i.e., the encoded *k*-space is identical for each time-slice and orthogonal to the time domain. However, a local gradient interferes with the phase encoding gradients and progressively shifts the origin of *k*-space along the direction of the local gradient during spectral encoding, as shown in Figure 3. The corresponding signal shifts in data space, which have been described as group spin-echo shifts in gradient echo imaging (10), shorten the measured signal decay along the spectral dimension and result in broadening of the reconstructed spectral lines. Linear gradients move the signal (and the origin of the encoded *k*-space) along a straight line toward the edge of the encoded data space whereas nonlinear gradients disperse the signal in data space. As a result of local gradients, *k*-space encoding is no longer orthogonal to spectral encoding and becomes a function of space and spectral-encoding time. Shimming aims at reversing the effects of local gradients by reversing the signal shifts in data space to restore time-invariant *k*-space encoding. Increasing spatial resolution increases the extent in *k*-space, which allows divergent signals from regions with magnetic field inhomogeneity to remain longer within the acquired data space, thus extending the measured signal decay and narrowing the spectral line width in these regions.

High-Speed MRSI

Acceleration of ^{1}H-MRSI is highly desirable to increase volume coverage, reduce motion sensitivity and decrease scan time, if SNR permits. High-speed MRSI methods are also advantageous for integrating high resolution MRS methods, such as correlation spectroscopy (COSY) (11) and J-resolved spectroscopy

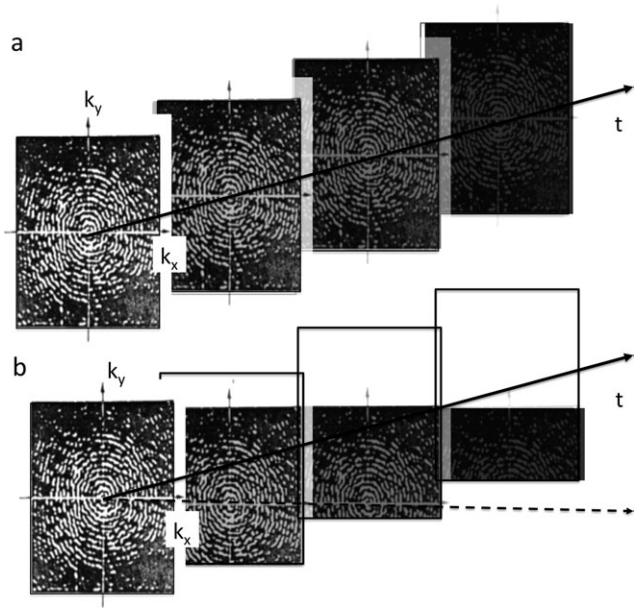

Figure 3. *K*-t-space in MRSI and effect of magnetic field inhomogeneity. **a**: *K*-space is invariant along the time axis in a homogeneous magnetic field. The decay of the encoded signals follows the time axis. **b**: *K*-space and the encoded signal move outside of the encoded data space due to a global gradient along the y-direction, which accelerates the signal decay and broadens spectral lines.

(12), for 3D spatial mapping of gamma-amino-butyric-acid (GABA) using spectral editing (13) and for implementing elaborate phase cycling schemes into MRSI. The rapidly expanding field of hyperpolarized MRI has invigorated the development of ultra-fast MRSI encoding schemes with the goals of minimizing image blurring and maximizing efficient use of the rapidly decaying magnetization (14,15). Many of the fast MRSI methods are based on high-speed MRI methods and largely fall into the following categories:

(i) Interleaving a series of repeated spatial readout modules during the spectral acquisition enables simultaneous encoding of spatial and spectral information with considerable increase in overall acquisition speed. The duration of the spatial readout modules determines the spectral with and the duration of the train of readout modules determines the spectral resolution. Echo planar spectroscopic imaging (EPSI), which uses interleaving of 1D, 2D, and 3D spatial echo-planar encoding into the spectroscopic acquisition, was one of the earliest high-speed MRSI approaches, originally developed by Mansfield (16) and later adapted for human applications (17–20). Advantages of EPSI include an adequate spectral width at field strengths up to 3 Tesla in the case of 1D echo-planar encoding, a high spectral resolution and high sensitivity comparable to conventional MRSI, and the relative ease of data reconstruction. Spiral MRSI, which uses interleaving of 2D or 3D spiral encoding during the acquisition, offers faster acceleration than EPSI due to the higher efficiency of the spiral trajectory (21) and provides flexibility in shaping the point spread function. However, data reconstruction is more demanding than for EPSI and requires correction for stronger off-resonance effects. Furthermore, the long duration of 2D and 3D encoding modules limits the spectral width that can be achieved in a single shot. Combination with echo time shifting (see below) can be used to expand the spectral width.

(ii) Shifting of the readout module position relative to the spin echo time (*echo time shifting*) in separate acquisitions is an alternate method for encoding of spectral information. The most basic application of echo shifting is the Dixon method, which separates water and fat (22). High-speed 2D imaging methods, such as EPI, rapid acquisition with relaxation enhancement (RARE) or spiral MRI, have been combined with echo time shifting to rapidly map brain metabolites (23,24). This approach is time efficient for applications that require only limited spectral resolution. However, achieving high spectral resolution and large spectral bandwidth is time consuming and decreases SNR per unit time.

(iii) Multiple spin echo acquisition with separate phase encoding of individual spin echoes has been developed to accelerate conventional MRSI (25,26). However, spectral resolution is reduced due to the shortened readout, and *k*-space weighting due to T_2 signal relaxation between the individual spin echo acquisitions needs to be corrected to minimize spatial blurring.

(iv) Parallel imaging using phased array coils has been applied to conventional (27) and high-speed MRSI (28,29) to achieve considerable acceleration of spatial encoding, including single-shot 2D encoding (30). However, increases in encoding speed need to be balanced with increases in noise due to the reduced acquisition time and g-factor related reconstruction errors that can compromise spatial localization and spectral quality. Recent developments using compressed sensing (15), and the combination of parallel imaging with compressed sensing (31), exploit the sparsity of spectral information to achieve even faster encoding speed, but the increase in encoding speed needs to be balanced with increases in g-factor related reconstruction errors.

(v) Steady-state free precession (SSFP) MRSI offers fast acceleration and high sensitivity per unit time, but the short spectroscopic readout requires sacrificing spectral resolution at 1.5T and 3T (32,33). SSFP methods are also sensitive to off-resonance effects, which may limit volume coverage. Recent studies combining SSFP-MRSI with echo-planar or spiral encoding and with parallel imaging have demonstrated very fast encoding speeds (34).

(vi) Sparse image-based *k*-space encoding schemes, such as spectral localization by imaging (SLIM) (35), and related approaches, have been proposed for situations where localization of a small number of arbitrarily shaped compartments is desired. These methods can be time efficient depending on the allowable amount of spatial crosstalk between these compartments. However, typical applications are aimed at minimizing cross-talk, which increases the number of encoding steps required.

(vii) Hadamard encoding has been introduced for applications where minimum voxel crosstalk is required (36,37). It makes use of multi-slice radiofrequency pulses with 0° or 180° phase shifts for each slice that change from encoding step to encoding step. A simple hadamard-encoded experiment that localizes two slices consists of one experiment in which the phases of the two slices are both 0° and a second experiment in which the phases of the two slices are 0° and 180°. Addition of the two data sets generates the signal of the first slice and subtracting the two data sets generates the signals of the second slice. However, the RF power requirements for multi-slice excitation limit this approach to small spatial matrix sizes.

To summarize, echo-planar and spiral encoding are the most commonly used high-speed MRSI methods

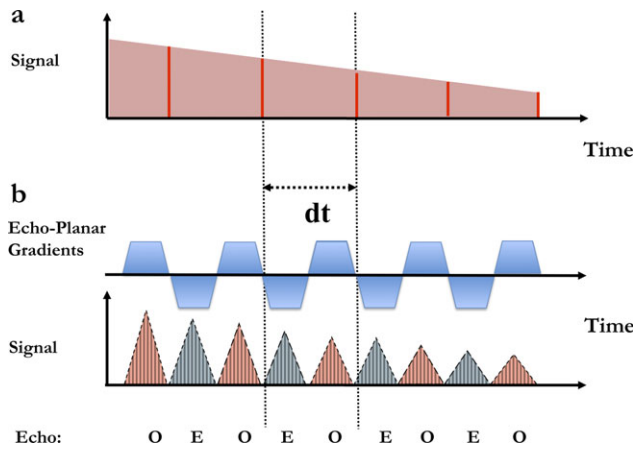

Figure 4. Echo-planar spatial-spectral encoding. **a**: Conventional MRSI acquisition with sampling points indicated by red lines. The spacing between sampling points is the spectroscopic dwell time (dt). **b**: Interleaving of pairs of echo-planar readout gradients into the spectroscopic acquisition creates a series of even and odd gradient echoes.

due to their high spectral quality and sensitivity per unit time and unit volume that are comparable to conventional phase-encoded MRSI, but with substantially enhanced temporal resolution (19,38). As echo-planar MRSI is of considerable interest for clinical applications, we now discuss this method in more depth.

Echo-Planar MRSI

^{1}H-MRSI using echo-planar encoding is increasingly used for brain research applications due to its robust localization performance and large volume coverage with much improved spatial and temporal resolution compared with conventional phase-encoded MRSI. The advent of echo-planar imaging (EPI) has greatly facilitated the implementation of echo-planar MRSI on conventional clinical MRI scanners. Echo-planar MRSI has been implemented at field strengths ranging from 1.5 to 7 Tesla (39,40). The feasibility of whole brain coverage has been demonstrated at intermediate and long TE (5,41–43). Proton echo planar spectroscopic imaging (PEPSI) is a development of echo-planar MRSI that enabled very short TE (e.g., 11 ms) for 2D and 3D spatial mapping of singlet and J-coupled metabolites in human brain with clinically feasible acquisition times of less than 5 min (8,18,19,29,39).

Echo-planar encoding can be conceptualized as follows: The relatively narrow spectral width of the proton spectrum (most resonances are within a 1 kHz range at 3 Tesla) is typically sampled with a spectroscopic dwell time on the order of 500 μs to 1 ms. This dwell time allows interleaving of echo-planar readout gradients with alternating polarity between spectroscopic data acquisition points (Fig. 4) to encode localized spectra that are spatially resolved in one dimension in a single excitation. Conventional phase encoding is used for the 2nd and 3rd spatial dimensions. The echo-planar readout gradient train, which encodes a zigzag trajectory in *k*-t-space, creates a series of gradient echoes that are modulated by chemical shift evolution and relaxation. Reformatting these data into a 2-dimensional matrix creates a data format that is equivalent to that of conventional phase-encoded MRSI. In practice, the even and odd echo data are not equivalent due to asymmetries in gradient switching, eddy current induced signal distortions and other factors, and direct Fourier transformation across even and odd echoes would lead to ghosting artifacts in the spectral domain. Although correction schemes for the shifts of the even and odd echoes have been developed to minimize ghosting in the frequency domain (20,40), separate reconstruction of the data from even and odd echo acquisitions has emerged as the preferred reconstruction method that avoids ghosting altogether (18). The flyback gradient scheme, which uses only the even gradients for spatial encoding and short gradient pulses with maximum slew rate for refocusing, has been proposed as an alternative approach to avoid eddy current effects and ghosting (41), but sensitivity is reduced due to gaps in data acquisition during the flyback gradient.

The PSF and the manifestations of magnetic field inhomogeneity in *k*-t-space are similar to those with conventional phase-encoded MRSI. Geometrical displacement artifacts due to the interference of local gradients with the echo-planar readout gradients are typically quite small due to the high amplitudes of the readout gradients. However, inhomogeneity-related signal displacements in *k*-t-space alternate along the readout direction for positive and negative echo-planar readout gradients, which leads to a zig–zag displacement of *k*-space along the time axis. Separation of even- and odd-echo data or the use of a flyback method avoids possible interference due to this zig–zag trajectory. EPSI is remarkably resilient against eddy current artifacts that predominantly manifest as distortions at the base of the spectral peaks. However, EPSI is sensitive to frequency drifts and spectral line broadening due to gradient heating, which may require frequency drift compensation (42).

Concerns have been raised regarding the sensitivity of EPSI, wherein the increase in acquisition bandwidth BW, which corresponds to the number of voxels X in the readout dimension, introduces noise ($\sim\sqrt{BW}$) that reduces the SNR compared with conventional MRSI. While this is true for an individual data trace, it must be borne in mind that the acquisition is accelerated by a factor of N. Increasing the acquisition time to that of conventional MRSI by using signal averaging increases SNR to that of conventional MRSI. In fact, sensitivity per unit time is similar to conventional phase encoding, provided that ramp sampling is used (38,43).

Volume Prelocalization

For most MRSI applications it is necessary to restrict the volume selection for the following reasons: (i) To avoid regions with strong static and radiofrequency magnetic field inhomogeneity that distort spectral lines and create distant spectral artifacts due to Gibbs

ringing. (ii) Constraining the acquired matrix size, in particular with conventional phase encoding, may be necessary to achieve clinically acceptable scan times. (iii) For brain MRSI, it is necessary to suppress overwhelming peripheral lipid and water signals to prevent spectral contamination inside the volume of interest, which requires robust prelocalization methods.

Single-shot selection of a rectangular volume of interest using point resolved spectroscopy (PRESS) (44) or stimulated echo acquisition mode (STEAM) (45) is the most robust and frequently used form of volume prelocalization. However, the positioning of a rectangular box selection within the brain prevents measurements in the lateral cortices and requires skill, because it does not conform to anatomical areas of interest. Outer volume suppression outside of the volume selection may be added to improve suppression of outside signals and to reduce the effects of chemical shift displacement and flip angle variation in the transition region at the edges of the volume selection, which for PRESS are particularly strong along the directions selected by the refocusing RF pulses. Adiabatic refocusing RF pulses, which are used in the localized adiabatic spin-echo refocusing (Laser) and semi-LASER MRSI pulse sequences (46,47), reduce chemical shift displacement artifacts and B_1-sensitivity compared with conventional refocusing RF pulses, although at the expense of increased RF power deposition and longer minimum TE.

Localization methods that are more comparable to conventional MRI, and extend volume coverage into the lateral cortices, include multi-slice acquisition (48) and slab selection with 3D encoding (18,49). These methods enable very short TE when using spin echo or stimulated echo excitation (8,18). For ^{1}H MRSI it is necessary to add outer volume suppression, frequency selective lipid suppression, lipid nulling, or a combination thereof, to suppress lipid signals from the periphery (see below). Multi-slice acquisition is often adequate for studies of the upper cerebrum, but the long spectroscopic readout at 1.5 and 3T limits the number of slices that can be measured within typical TRs of 2–3 s unless spectral resolution is sacrificed (50). Multi-slice acquisition is attractive at 7T, because the duration of the spectroscopic signal acquisition is shorter and slice-specific dynamic shimming can be integrated (51). Selection of a thick slab with 3D encoding enables greater volume coverage, higher spatial resolution in the slice direction and at 1.5 and 3T it is SNR efficient compared with multi-slice acquisition. However, chemical shift displacement and flip angle variation in the transition region at the edges of the slab leads to chemical shift dependence of the resonance amplitudes and complex J-modulation patterns, which reduces the number of useable slices. Due to RF power constraints, the RF bandwidth of the excitation RF pulse is usually larger than that of the refocusing RF pulse, which further complicates J-modulation at the edges of the slab. In regards of this consideration, the use of adiabatic refocusing RF pulses is advantageous, because they reduce chemical shift displacement artifacts and also minimize the effects of B_1-inhomogeneity across large volumes.

Outer volume suppression (OVS) using spatial presaturation (52–56) provides flexibility in shaping the volume of interest and for the brain allows measurement of the lateral cortices, which is not feasible with PRESS or STEAM prelocalized MRSI. Overall lipid suppression, although less efficient than with PRESS or STEAM prelocalization, is adequate for most MRSI applications, if a sufficiently high spatial resolution is used to limit lipid contamination due to the point spread function to voxels in the periphery (8). Furthermore, model-based spectral fitting, for example using a linear combination of model spectra (LCModel) (57), is quite tolerant to baseline distortions due to residual lipid signals. However, chemical shift displacement and flip angle variation in the transition region at the edges of the OVS slices need to be considered when positioning the OVS slices, which favors narrow OVS slices for suppressing peripheral lipid containing regions. Challenges of outer volume suppression include compensation of T_1 related signal recovery during the application of a large number of suppression RF pulses, compensation of B_1 sensitivity and minimization of signal refocusing due to secondary echoes at the intersection of the suppression slices. OVS can also be applied during the mixing time (TM) period in a STEAM pulse sequence (18) and in the form of Spatially Selective Echo-Dephasing (SSED) RF pulses that are inserted around the refocusing RF pulse(s) in a spin echo or PRESS pulse sequence (58). These approaches reduce sensitivity to T_1 dispersion among lipid signals and B_1 inhomogeneity. When combined with presaturation they provide strongly enhanced overall lipid suppression performance. State-of-the-art OVS method development has focused on improving the suppression efficiency by optimizing RF pulse design (59), gradient switching schemes and timing of OVS modules, and localized tuning of individual OVS RF pulses (19). Recently, Henning et al developed powerful T_1- and B_1-insensitive outer volume suppression methods with highly selective broadband RF pulses to minimize chemical shift displacement artifacts at high field (60,61).

A major challenge of spatial lipid suppression approaches is that precise (manual) placement of a large number of OVS slices to cover peripheral regions while minimizing loss of cortical signals is required, which can also introduce operator-dependent and inter-subject variability of the VOI. Manual placement of OVS slices requires considerable skill and time to balance the needs of completely covering peripheral brain regions with a limited number of OVS slices (to constrain T_1-related losses in suppression) and minimizing the loss of lateral cortical brain regions while taking into consideration the OVS slice transition bandwidth and chemical shift artifacts. Semi-automated and automated methods for OVS placement that are based on anatomical landmarks or segmentation of high resolution MRI have been developed (Duyn et al [48], Venugopal et al [62], Ozhinsky et al [63]). We have proposed an iterative optimization approach to automatically place up to sixteen OVS slices in peripheral regions using image segmentation (64). These automatic methods are capable of

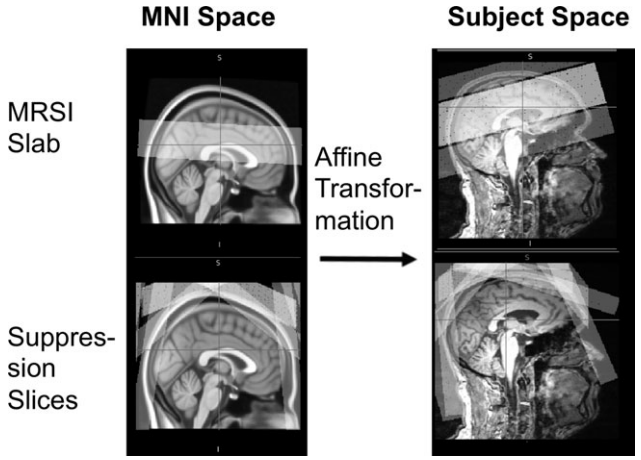

Figure 5. Automated prelocalization of the MRSI volume of interest in reference to a brain atlas. The MRSI slab and outer volume suppression slices are optimally positioned in the Montreal Neurological Institute brain atlas. An affine transformation based on the spatial normalization of the subject's brain into the atlas space enables automated placement of the MRSI slab and outer volume suppression slices in subject space.

accurate placement of OVS slices on a subject-by-subject basis, but they are sensitive to brain segmentation errors and local minima in optimization, which affects reliability and consistency, and they are still time consuming to apply in the clinical setting. Motivated by the increasing availability of statistical brain atlases for automated positioning of MR imaging slices, and the proven high efficiency, robustness and precision of this methodology (65,66), we recently introduced a brain atlas-based approach for automated positioning of up to 16 OVS slices that uses an affine transformation of optimally positioned OVS slices and the MRSI slab in atlas space (4) (Fig. 5), which is comparable in lipid suppression performance to the iterative optimization approach, but faster. In the future, a nonplanar geometry of automated OVS slice prescription from nonlinear transformation may be feasible using curved slice excitation with multidimensional RF pulses (67) to improve volume coverage in lateral brain regions.

The STIR method (7) avoids the complications of volume preselection in whole brain ^{1}H-MRSI and enables encoding of metabolite signals in the lateral cortices in close proximity to peripheral lipid-containing regions (68). However, an approximately 30% sensitivity loss in all metabolites is incurred at 3T and elevated lipid and macromolecular resonances that are valuable for assessing brain lesions are not measurable. Furthermore, the efficiency of lipid nulling is limited by the T_1 dispersion between lipid resonances, which makes this method most suitable for intermediate and long echo time (TE) acquisitions, although implementations for short TE acquisition are under development (see Integration into Clinical Routine). The signal losses in the major metabolite resonances can be minimized using a frequency-selective inversion recovery method that selectively inverts the major lipid peaks (69). Frequency-selective suppression using RF band selective inversion with gradient dephasing (BASING) (70) has been proposed as an alternative and implementations have shown powerful suppression performance. However, disadvantages of these techniques include a substantial increase in minimum TE, suppression of lactate and macromolecular signal originating from brain tissue and increased sensitivity to static magnetic field (B_0)- and RF field (B_1) inhomogeneity that limit volume coverage.

Standardization of volume prelocalization between manufacturers is necessary to increase clinical acceptance of MRSI. Reproducible and automated prelocalization of major parts of the cerebrum and the cerebellum with negligible contamination from peripheral lipids and acceptable spectral line width should be the focus of such standardization.

Water Suppression in 1H MRSI

T_1- and B_1-compensated multi-pulse water suppression schemes, such as water suppression enhanced through T1 effects (WET) (71) and water suppression with variable power RF pulses and optimized relaxation delays VAPOR (72), are necessary to reduce the broad baseline of the water signal, to minimize gradient sideband artifacts and to avoid Gibbs ringing of frequency shifted water signals from regions with static magnetic field inhomogeneity. Static magnetic field inhomogeneity across large volumes requires increases in the water suppression bandwidth and leads to local frequency-shift dependent suppression of resonances in the vicinity of the water peak. In practice, the residual water peak is distorted and varies spatially in amplitude, which leads to substantial baseline variability that impairs metabolite quantification. Spatial-spectral water suppression pulses that can be applied in a slice selective manner allow for narrower water suppression bandwidth for applications using multi-slice MRSI sequences (73). Simultaneous measurement of signals from unsuppressed water and metabolites, a recent development which has been demonstrated for SV-MRS using high dynamic range digital receivers (74–76), would be desirable to avoid the complications of spectrally-selective water suppression and to enable direct spectral quantification without a reference scan, but the technical challenges are considerable.

SPECTRAL QUANTITATION

This section summarizes general approaches for quantifying MRSI data; there are recent reviews available that provide detailed assessments of SV-MRS and MRSI analytic approaches (3,77). The goal is to transform the signal intensity measurement into a measure of tissue metabolite concentration referenced to the volume (mol/mL) or the mass (mol/g) of tissue being studied. It could also refer to the volume, mass or amount of water in the tissue being studied. Tissue quantification typically requires a tissue content analysis (78). For instance it is usually assumed that cell-

free body fluids (e.g., ventricles or sulci in the brain) produce no metabolite signal and such regions should not be included in the concentration estimation. Partial volume correction, based on tissue masks from high resolution MRI that are convolved with the MRSI PSF to determine the water fraction of a particular voxel, is used to compute metabolite concentrations.

MRSI quantitation is typically performed separately for each voxel in the reconstructed data set as a straightforward extension of techniques developed for SV-MRS. With MRSI the number of voxel spectra are so large that automated methods for spectral preprocessing and spectral fitting are required (79). For instance, local frequency shifts due to inhomogeneous B_0 field require correction to avoid errors in spectral assignment, which is challenging in the presence of regionally varying spectral patterns and low SNR. The problem is exacerbated when there are lesions present that produce uncharacteristic spectra and when nuisance signals, such as poorly suppressed water signal or lipid signal in ^{1}H-MRSI, distort the spectrum. For ^{1}H-MRSI, an unsuppressed "water reference" MRSI scan is usually obtained as a reference for spectral quantification and to measure the spatial distribution of the B_0 field, which can be used to correct the frequency offsets of each of the voxel spectra in the water suppressed MRSI measurement. The phase of the water reference MRSI can also be used to correct the zero order phase in the water suppressed spectra. However, the water signal may not be usable as a reference in all tissue compartments. For instance, in the breast the water signal in adipose tissue may be very small.

The use of array coils introduces coil dependent signal strength and phase characteristics in each spectrum. It remains somewhat controversial how to optimally recombine the spectral information arriving from each of the array elements although several approaches have been proposed (80–83). Knowledge of what combination procedure was used can be important if measures of different voxels from an MRSI data array are being compared or if the study involves across-subject quantitation. Spectral quantification should also take into consideration chemical shift dependent signal attenuation due to chemical shift displacement at the edges of the volume selection, and flip angle variations across the volume selection, which change J-coupling patterns, but this is technically challenging.

Quantitation must include correction for T_1 related signal saturation and T_2 relaxation of the metabolite signals and the water reference signal in the different tissue compartments, which is derived from the pulse sequence timing and RF pulse characteristics that the pulse sequence uses (8,84). The MRSI PSF is used for correcting relaxation effects in different tissue compartments within a voxel. Ideally, T_1 and T_2 of the relevant metabolite signal should be measured on an individual basis to avoid a biased metabolite concentration determination (85–87), but this is rarely performed in clinical MRSI studies due to time constraints. Some calibration approaches report only normalized concentration, which is equivalent to the true concentration multiplied by a relaxation factor (68,79). An alternate strategy is to reduce the impact of T_1 relaxation correction by using long TR, which is feasible with high-speed MRSI at the expense of only minor reduction in sensitivity, and to use short TE to reduce the effects of T_2 relaxation.

Absolute concentration estimates are usually obtained by calibration of the measured metabolite signal against a reference signal produced by a material having a known concentration because MRI scanners are generally not designed to measure absolute signal levels. The reference signal for spectral quantitation may be generated by a metabolite, by water or by some other chemical compound in a phantom object (88). Calibration using near-tissue phantoms (i.e., phantoms that are outside the subject's body and imaged together with the subject) is used infrequently due to several practical implementation problems related to B_0 inhomogeneity and B_1 inhomogenity. Calibration using a signal produced by a replacement phantom object, which is imaged before or after the subject examination, avoids some of the practical problems associated with using near-tissue phantoms, but can also have pitfalls related to differences in coil loading and to relaxation time differences between the metabolite signal and the reference signal. Calibration against an internal signal (i.e., one that is produced by the tissue but has a reasonably well known concentration or is assumed to be unchanging) is, therefore, used in most studies. Typically, the internal reference signal used in ^{1}H-MRSI is either the principal Creatine (Cr) signal (3.05 ppm) or the water signal (4.69 ppm). However, disease related changes in Cr and tissue water might bias quantification. If the water signal is used as a calibration signal, its amplitude must be measured by performing a separate MRSI study without water suppression, which is time consuming with conventional MRSI, or by interleaving the reference scan into the water-suppressed scan. Fast MRSI acquisition technology enables rapid acquisition of reference scans for both long TE MRSI (79,89) and short TE MRSI (8). One useful feature of MRSI is that the reference signal can come from any tissue region from within the imaged field of view, provided that transmit and receive sensitivities are spatially uniform or known from prior sensitivity measurements. This enables the investigator to, for instance, calibrate the entire data set against a reference signal measurement made in a tissue region that appears normal on MRI and is not involved in the disease process under study. More accurate quantification also requires correction for differences in NMR visibility of tissue water in different tissue types using tissue segmentation based on high resolution MRI (e.g., gray and white matter regions in the brain).

The choice of method to determine the signal amplitude in MRSI studies has typically depended on the degree of spectral complexity, the signal overlap within individual voxel spectra and the degree of spectral artifacts. For long-TE ^{1}H-MRSI, J-modulation and T_2 signal decay tend to produce a situation in which only the prominent singlet signals can be detected above noise and straightforward signal

integration can be used to obtain signal amplitude. For carbon-13 (^{13}C)-MRSI, the signals of interest are usually well enough separated due to the excellent chemical shift dispersion of ^{13}C-MRS that straightforward signal integration can also be used. For short TE ^{1}H-MRSI and phosphorus-31 (^{31}P)-MRSI, it has become commonplace to assume that the tissue spectrum is represented by a "spectrum model", which is the sum of many complex-valued signals arising from many metabolites. "Optimization" or "fitting" software is then used to repetitively adjust the frequencies, phases and amplitudes of the signals until a simulated model that agrees with the observed data is found. Typically, spectral fitting techniques make use of well-established least squares optimization procedures that are used to solve analogous optimization problems in other scientific and engineering fields. The spectral models used by these software packages fall into two broad categories (90). The model may be a group of individual signals each of which has its own signal frequency, peak width, phase and amplitude. An alternative approach, which was first implemented by LCModel for in vivo ^{1}H-MRS, uses a model that recognizes that the individual metabolites are most correctly modeled as a singlet and multiplet pattern of signals produced by each proton in the molecule (57). Spectral fitting approaches operate either in the time domain (79,91–95) or the frequency domain (96–99). Most of these software packages were developed for SV-MRS at a time before MRSI was widely available. The most popular spectral fitting software is currently LCModel (57). It uses a Bayesian approach to include prior information (e.g., soft constraints for lipids and macromolecules) and regularization of baseline estimation to stabilize fitting results in the presence of spectral artifacts from residual water and lipid signals. It also uses Bayesian learning to get starting estimates and "soft constraints" for the first-order phase correction and the frequency shift from the preceding (often better) central voxels or the (often poorer) outer voxels.

Region-of-interest analysis using averaging of single voxel results, which capitalizes upon the large number of voxels obtained using MRSI, can substantially improve sensitivity. It has been shown that averaging the raw data from individual voxels before applying LCModel fitting provides improvement in SNR compared with averaging concentration values from individual voxels, which is a result of reduced bias in baseline estimation and spectral fitting of J-coupled resonances when increasing the SNR in the raw data (100). However, spatial correlations between spectra as a result of the point spread function and spatial filters may limit actual gains in SNR.

The results of MRSI quantification are thus often still examined by visual inspection of the localized spectra on a voxel-by-voxel basis, which is time consuming and may create bias. This approach also makes interpretation of regional differences in metabolite concentration and referencing to anatomy difficult. Recent advances in high-speed ^{1}H-MRSI provide sufficient spatial resolution to allow reconstruction of metabolite images with coarse anatomical features that can be referenced to high resolution MRI. For between-group studies it is necessary to spatially transform metabolite images into a common anatomical reference frame represented by a brain atlas (101), which requires the use of 3D MRSI.

Color-coded metabolite images can be overlaid on high-resolution MRI for visualization. Image interpolation is usually applied to make the metabolite maps acceptable for viewing, but the introduced spatial smoothing may be misleading. Furthermore, metabolite maps may have a very large dynamic range, which is difficult to display. Standardization of spectral processing and display of metabolite maps between manufacturers is necessary to increase clinical acceptance of MRSI. Deconvolution of the baseline and fitting of overlapping multiplet resonances at short echo times are particularly challenging and critical processing steps. These processing steps are handled differently by the various MRS processing packages and should be the focus of such standardization.

Quality control is an important aspect of MRSI. Physiological motion may produce variations in signal phase and frequency, which reduces the expected SNR enhancement during signal averaging due to destructive averaging, and it creates ghosting in the phase encoding direction(s) that may lead to unexpected spectral artifacts anywhere in the spectroscopic images. Efforts to address this problem using motion correction based on navigator signals have recently been published (102–104).

INTEGRATION INTO CLINICAL ROUTINE

Spatial Resolution, Volume Coverage, and Spectral Specificity in the Brain at 3T

MRSI has been most successful in the brain due to favorable field homogeneity conditions, the ease of immobilizing the head and highly sensitive signal detection using close fitting volume coils and surface coil arrays. We highlight advances in echo-planar MRSI using PEPSI and related techniques, because these are representative for the current state-of-the-art of ^{1}H MRSI techniques at 3T.

The high sensitivity of ^{1}H-MRSI and use of sensitive surface coil arrays in combination with high-speed MRSI enables metabolite mapping with the spatial resolution approaching that of functional MRI to delineate gray–white matter differences in metabolite concentration. Figure 6 shows examples of mapping J-coupled resonances with 4.5 mm in-plane resolution using PEPSI at short echo time (15 ms) in a healthy volunteer. The combined Glutamate+ Glutamine (Glu+ Gln) map shows gray–white matter contrast, which follows the sulcal pattern seen in the corresponding high resolution MRI. The Cr map also shows gray–white matter contrast and the Choline (Cho) map shows an inverse contrast as well as higher Cho concentration in anterior brain regions compared with the posterior brain.

Maudsley and colleagues have developed clinically feasible whole brain metabolite mapping for brain using 3D EPSI at intermediate echo times (70 ms) with scan times of 26 min (68,101). Figure 7 shows

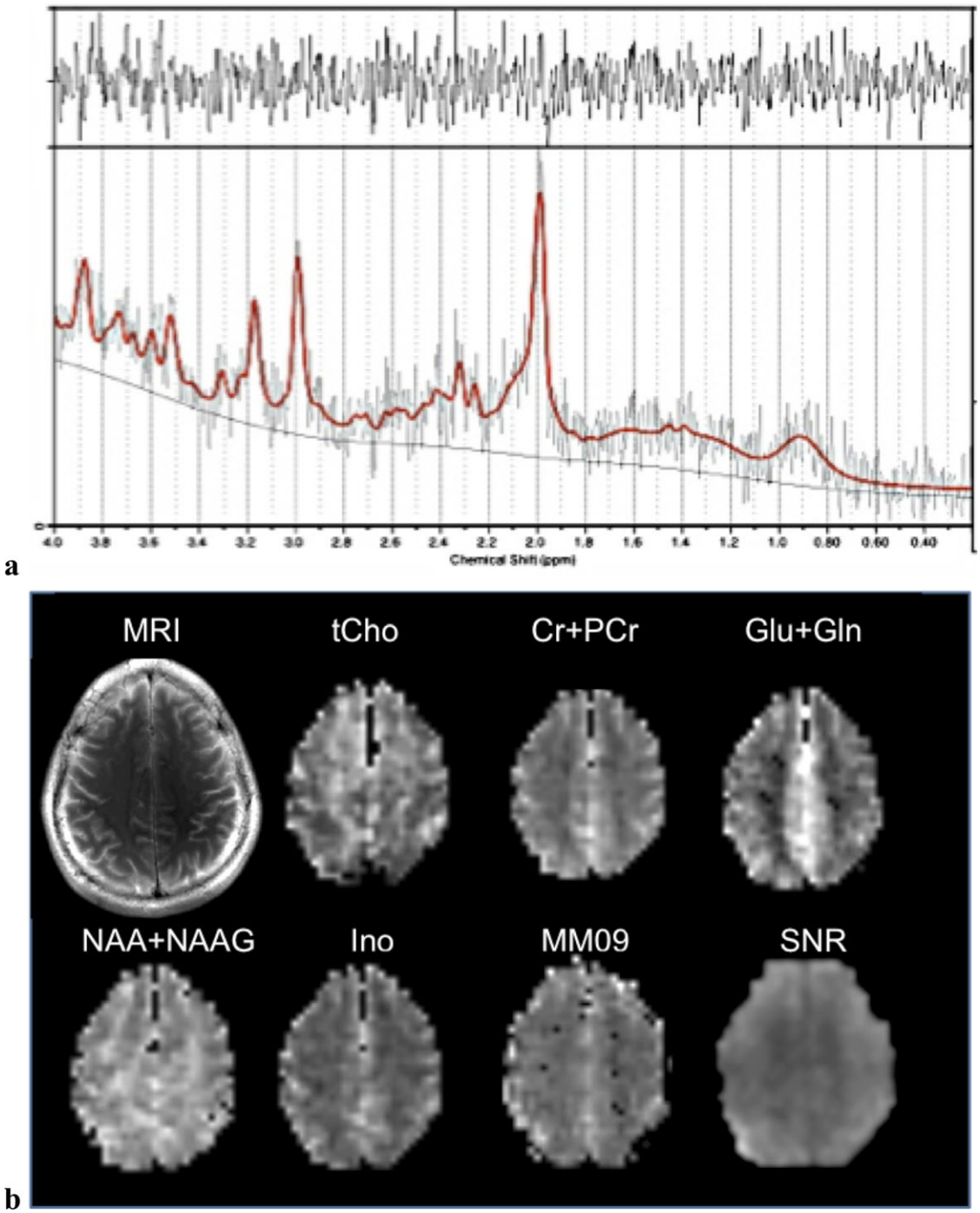

Figure 6. High spatial resolution mapping of J-coupled metabolites in human brain at 3 Tesla using short TE (15 ms) proton-echo-planar-spectroscopic-imaging (PEPSI). **a**: Localized spectrum in central gray matter with spectral fit using LCModel software (red). **b**: High-resolution MRI, partial volume and relaxation-corrected metabolite images, and signal-to-noise-ratio map (SNR). Data were acquired with 4.5 mm in-plane resolution and 15 mm slice thickness (0.3 cc voxel size) in a supraventricular slice location using a 32-channel array coil and 32 min acquisition time. [Color figure can be viewed in the online issue, which is available at wileyonlinelibrary.com.]

examples of metabolite maps measured in a single subject at intermediate TE and averaged results from a group study, which dramatically increases sensitivity and reveals previously unattainable tissue contrast in metabolite maps. Figure 7 also shows preliminary results from the same laboratory that demonstrate the feasibility of whole brain mapping at short TE (20 ms).

Mapping of neurotransmitters, such as Glu and GABA, is of considerable interest for characterizing neurological and psychiatric disease. The Glu multiplet is strongly overlapping with the Gln multiplet at 3T, and even at 4T, when line broadening is present, which makes it difficult to obtain independent concentration estimates for each of these molecules, although their sum (labeled Glx) can be estimated.

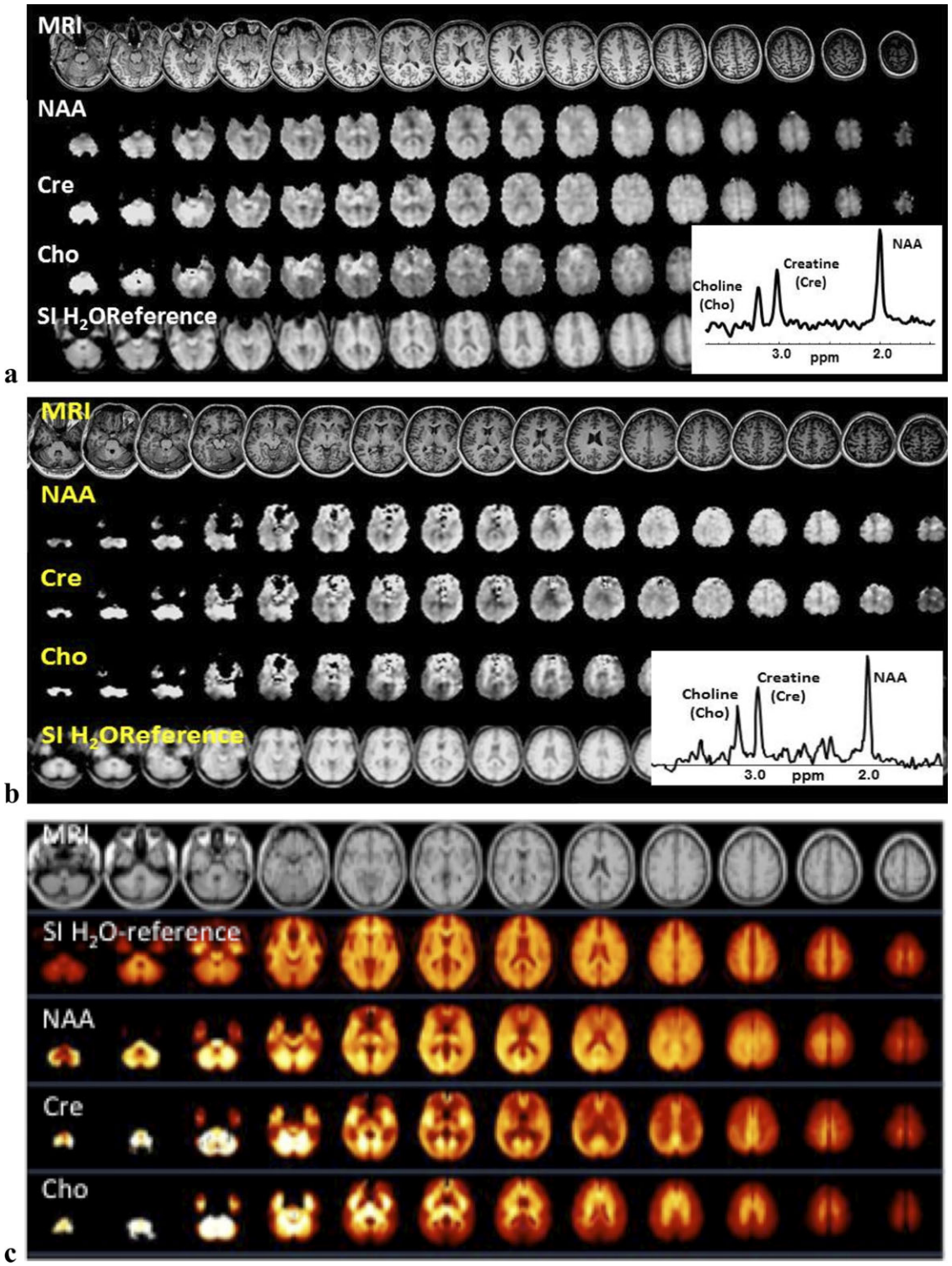

Figure 7. Whole brain mapping of metabolites using echo-planar-spectroscopic-imaging (EPSI) at 3 Tesla (68). **a**: Single subject at intermediate echo time (70 ms), (**b**) single subject at short echo time (20 ms) and (**c**) group average from 47 female and 41 male subjects at intermediate echo time (70 ms). Spatial normalization was applied. Intermediate echo time data were acquired using a 12-channel coil and 26 min acquisition time, with 50 × 50 × 18 *k*-space points interpolated to 64 × 64 × 32 and 5.6 × 5.6 × 10 mm (0.31 cc) voxel size. Short TE data were acquired in 15 min. (Adapted from: Mapping of brain metabolite distributions by volumetric proton MR spectroscopic imaging (MRSI). Maudsley AA, Domenig C, Govind V, Darkazanli A, Studholme C, Arheart K, Bloomer C. Magn Reson Med 2009;61:548–559. Copyright © 2008 by John Wiley and Sons, Inc. Reprinted by permission of John Wiley and Sons, Inc.). [Color figure can be viewed in the online issue, which is available at wileyonlinelibrary.com.]

a

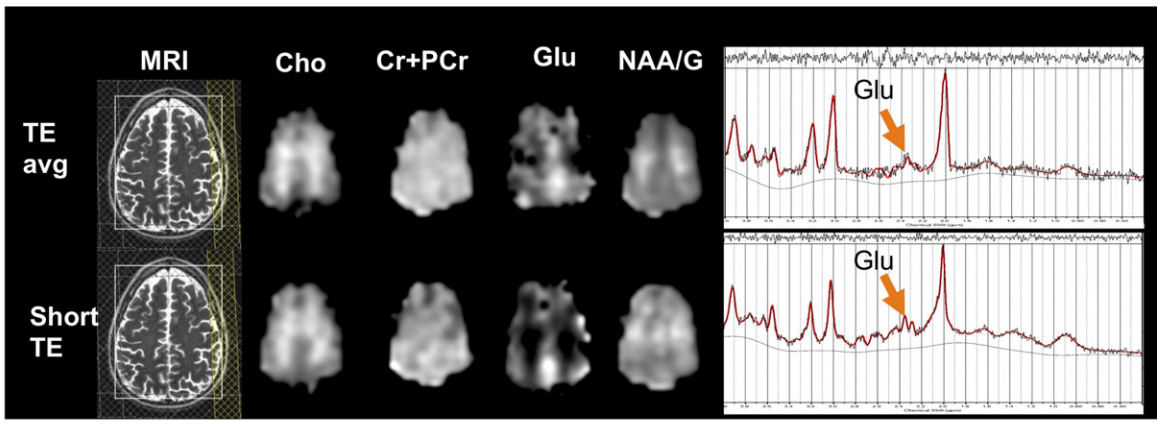

b

		Cho/Cr	Cr	Glu/Cr	NAA/Cr
TEavg	Concentration ratio	0.16	1	0.6	2.38
	CRLB [%]	23.4	8.3	23.9	7.2
	Voxels	238	294	231	302
	FWHM [ppm]	0.054			
	SNR	10.2			
Short TE	Concentration ratio	0.24	1	0.9	1.72
	CRLB [%]	12.7	7.5	16.8	6.74
	Voxels	290	301	274	301
	FWHM [ppm]	0.055			
	SNR	12.8			

Figure 8. The 3D glutamate mapping in human brain comparing TE-averaging versus short TE acquisition at 3 Tesla. **a**: MRI, metabolite maps and central spectra with spectral fit using LCModel software. **b**: Quantification of metabolites in central slice showing slice averages of metabolite ratio with respect to Cr, Cramer-Rao lower bounds (CRLB), number of voxels above a CRLB threshold of 50%, spectral line width and signal-to-noise-ratio. TE averaged 3D PEPSI data were acquired with TR: 1.5 s and 8 echo times ranging from 15 to 165 ms with 20 ms steps using 27-min 30-s scan time. Short TE (15 ms) 3D PEPSI data were acquired with TR: 1.5 s, 4 averages and 13 min 48-s scan time. Spectral fitting was performed with simulated basis sets. [Color figure can be viewed in the online issue, which is available at wileyonlinelibrary.com.]

MRSI studies of Glu have used spectral fitting at short TE (105), J-refocused coherence transfer (106), and more recently, 2D J-resolved MRSI using TE-averaging (12), which enables selective mapping of Glu. However, the wide range of echo times in TE-averaged MRSI limits the sensitivity gains at high field, as metabolite T_2 values decrease with field strength, and they are time consuming to perform with conventional phase-encoded MRSI. Echo-planar MRSI techniques have emerged as the preferred approach to reduce the long encoding times of TE-averaged MRSI (12,107). Figure 8 shows a comparison of TE-averaged 3D PEPSI with short TE 3D PEPSI at 3T. A 3D acquisition with slab-selection was chosen, because selecting a central slice within the slab avoids chemical shift displacement and flip angle variation at the edge of the MRSI slab that change J-coupling patterns and reduce sensitivity for detecting Glu. Data were acquired using identical voxel size (1 cc), but 2 times longer acquisition time for TE-averaged PEPSI due to the large number of TE averaging steps required. Despite the longer acquisition time of TE-averaged PEPSI, the Cramer-Rao lower bounds (CRLBs) for Glu were significantly larger than for short TE PEPSI and the number of voxels with Glu above threshold in the TE-averaged data was significantly smaller than for short TE data. Short TE acquisition thus provides higher sensitivity for mapping Glu in clinical studies, but spectral overlap with Gln in regions with spectral line broadening can compromise spectral specificity. TE-averaged acquisition is complementary to short TE acquisition for selectively mapping Glu, albeit at lower spatial resolution and/or longer measurement times.

Noninvasive and quantitative mapping of regional GABA concentrations in human brain by means of MRSI is an important development for noninvasive study of biochemical pathways in neuropsychiatric and neurological disorders and mechanisms of treatment. On clinical 3 T MRI systems, single voxel MEGA-PRESS has gained in popularity over the past years as an editing technique and has become available as a research package on most MR scanners. Feasibility of spectroscopic imaging with multi-quantum filtering (MQF) (108), two-dimensional J-spectroscopy (109) and J-difference editing has been demonstrated (110). However, these approaches have been limited to a single slice due to the use of conventional phase-encoding. Recently, using a combining

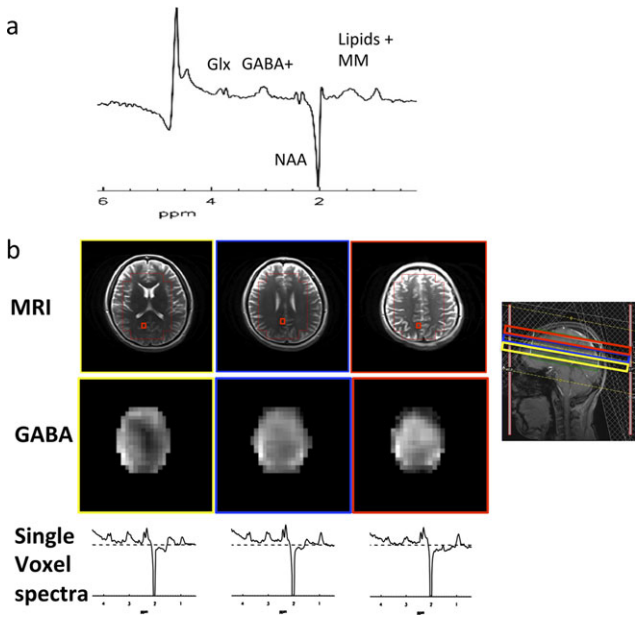

Figure 9. The 3D mapping of GABA in human brain using PEPSI with MEGA-editing at 3 Tesla. **a**: Difference spectrum from supraventricular gray matter with spectral assignments. **b**: GABA maps from 3 slices within the MRSI slab and representative spectra from voxel locations shown in the axial MRIs. Acquisition parameters: TR/TE: 2 s/68 ms, spatial matrix: 32 × 32 × 8, voxel size: 1.5 × 1.5 × 1.5 cm^3, scan time: 18 min. [Color figure can be viewed in the online issue, which is available at wileyonlinelibrary.com.]

the MEGA editing scheme with the PEPSI spatial-spectral encoding method enabled 3D GABA mapping with a 3.4 cc voxel size and 18 min of scan time, demonstrated in Figure 9 (13).

Clinical MRSI Applications in Brain

There are substantial benefits from using MRSI methods for clinical investigations that include rapidity of data acquisition from multiple anatomical regions simultaneously that allows both systematic appraisal of anatomical relationships to symptom expression and ease of application for difficult to examine clinical populations. Rapid ^{1}H-MRSI methods, such as PEPSI, enabled 2D and 3D regional mapping of dynamic metabolic changes in human brain in response to robust physiological challenges such as hyperventilation (39) or the more subtle metabolic effects of caffeine ingestion (111) on a time scale of minutes.

^{1}H-MRSI has been extensively used for diagnosis and treatment-follow up of brain tumors. Most of the published studies have used 2D MRSI at short and long TE, and 3D-MRSI at long TE. Figure 10 shows preliminary results of 3D metabolite mapping at short TE (15 ms) in a patient with an oligodendroglioma using the PEPSI technique with 7 mm isotropic spatial resolution and 10-min scan time including the water reference scan. The data show a typical tumor spectrum in the anterior part of the lesion, strong lipid signals in a more posterior section of the lesion, and edema characterized by high water concentration and narrow spectral line width further posterior to the lesion. The short scan time of the PEPSI method enabled integration into a multi-modal presurgical mapping protocol that included high resolution MRI (MPRAGE and T2-TSE), diffusion tensor imaging, tas*k*-activation fMRI, resting state fMRI and a GABA edited 2D PEPSI scan.

Brain MRSI studies have sought to investigate the underlying pathophysiology for a variety of neurological and psychiatric disorders, as recently reviewed (112). One such investigation, currently underway, is the application of 3D MRSI techniques to characterize the changing pattern of regional brain tissue metabolite levels longitudinally in infants at high genetic risk for autism spectrum disorder (ASD). ASD is a common developmental disorder estimated to affect up to 1 percent or more of individuals worldwide (113). It is currently diagnosed on the basis of behavioral manifestations of severe social and communication deficits and ritualistic-repetitive behaviors that are typically detectable in early childhood and continue throughout the lifespan. There is substantial interest in applying imaging modalities to understand the neuropathology underlying symptom expression and to identify biomarkers for early diagnosis that might allow targeted early intervention, shown to be useful for altering the course of ASD. An intriguing MRI finding from studies of preschool-aged children with ASD is the identification of cerebral enlargement of 9–12% as the most characteristic brain structural finding at that early age. In conjunction with cerebral enlargement, widespread anatomical distribution of metabolite alterations are observed, primarily reduced brain chemical concentrations per unit tissue volume, and prolonged metabolite T_2 relaxation, that are inconsistent with earlier theoretical models of abnormal apoptotic mechanisms that would predict diffusely increased neuronal packing density in young children with ASD (114,115). As reviewed recently (116), MRS patterns of abnormal chemical levels found in many studies of ASD, particularly reduced n-acetyl-aspartate (NAA), suggest differences in neuronal integrity or density that could reflect pathological process, such as intracellular inflammation, that may impact synaptic function, potentially in conjunction with specific genetic vulnerabilities. An example short TE 3D PEPSI data set (32 × 32 × 8 matrix - acquisition time of 5.5 min) and a 2D GABA-edited PEPSI data set (32 × 32 matrix – acquisition time of 8.5 min) measured in a 13-month-old at high-risk for ASD are shown in Figure 11.

Metabolite Mapping in the Breast

The addition of a total Choline (tCho) measurement using SV-MRS to a standard MRI workup of breast cancer was reported to improve lesion characterization, thus improving the limited specificity of dynamic contrast enhanced (DCE) MRI (117). SV-MRS has also been used in patients undergoing neoadjuvant chemotherapy to predict treatment response (118). MRSI has the potential advantage over SVS of assessing lesion heterogeneity and regional treatment response, which is advantageous in

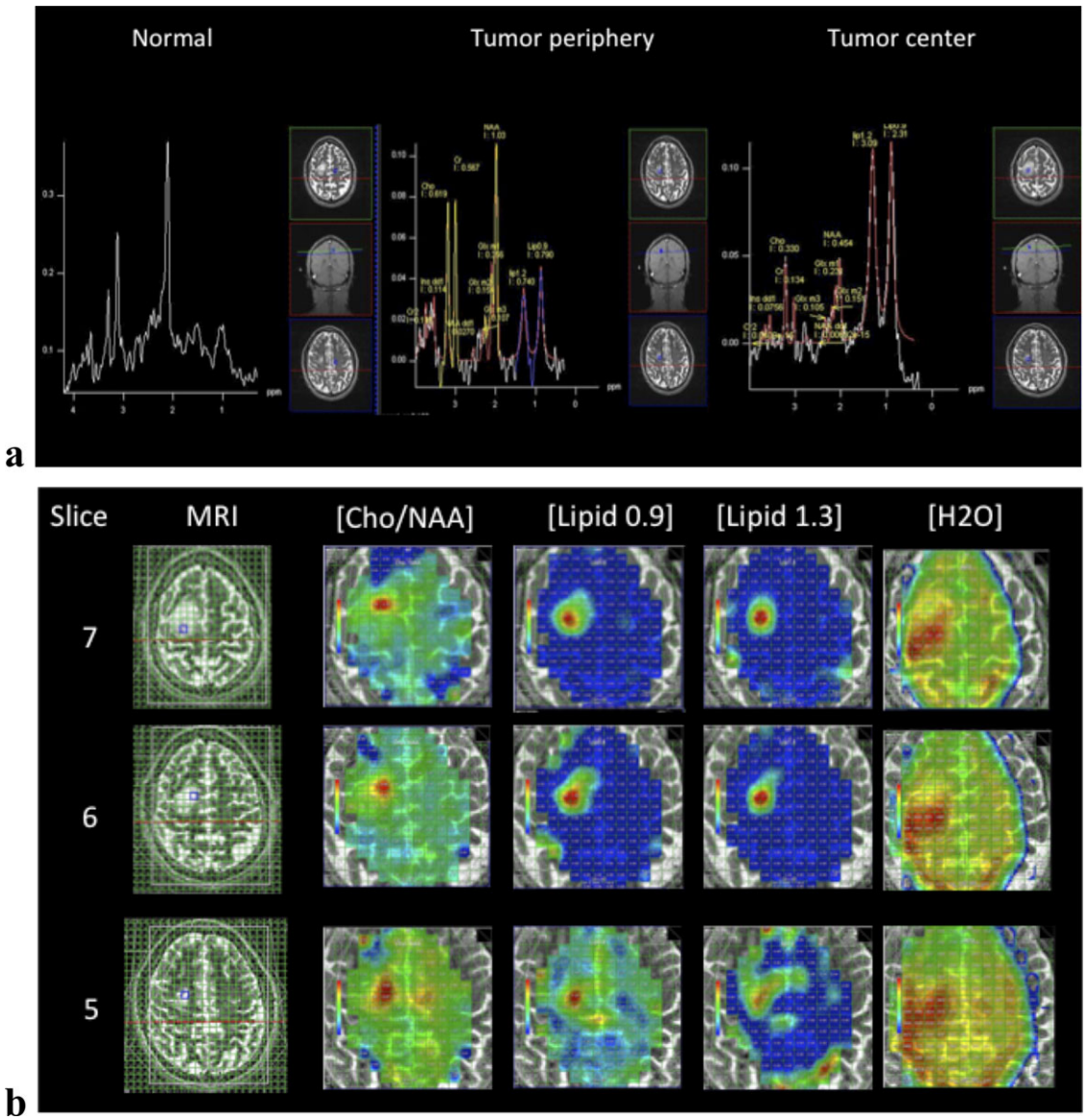

Figure 10. The 3D metabolite mapping in a patient with a brain tumor at 3 Tesla using short TE (15 ms) PEPSI. **a**: Localized spectra in the periphery of the tumor show elevated Choline and lipid peaks. Decreased Creatine and NAA, and strongly elevated lipid peaks are measured in the center of the tumor. **b**: T_2-weighted MRI, metabolite maps and water reference scan demonstrate spatial heterogeneity of the lesion. Data were acquired in 10 min including water reference scan using 32 × 32 × 8 spatial matrix and 7 mm isotropic voxel dimensions (0.34 cc voxel size). [Color figure can be viewed in the online issue, which is available at wileyonlinelibrary.com.]

multi-focal and multi-centric disease. However, the strong magnetic field inhomogeneity in the breast and the small water peak in adipose tissue make shimming across the entire breast challenging. Most studies using MRSI have, therefore, used PRESS volume preselection around the lesion(s) to maximize spectral quality, which, however, limits volume coverage. Furthermore, magnetic field inhomogeneity changes due to respiration introduce periodic frequency shifts that create ghosting artifacts, necessitating the use of navigator-based correction of frequency changes. Using PEPSI and a custom-designed spectral quantification method at 3 Tesla, Figure 12 shows an example of 3D mapping of tCho in a patient with biopsy confirmed multi-focal invasive ductal carcinoma grade 3 (119).

A recent study using heteronuclear MRS at 7 Tesla demonstrated the feasibility of monitoring neoadjuvant chemotherapy using 3D ^{31}P MRSI to map adenosine and other nucleoside triphosphates, inorganic phosphate, phosphocholine, phosphoethanolamine and their glycerol diesters, which were detected in glandular tissue as well as in tumor, over the entire breast (120), as shown in Figure 13.

Metabolite Mapping in Prostate and Other Organs

Over the past few years, MRSI has emerged as a useful complement to structural MRI for evaluation of prostate cancer (121). MRS-detectable cancer biomarkers and biochemicals in the prostate include citrate, creatine, polyamines, and choline. In spectra

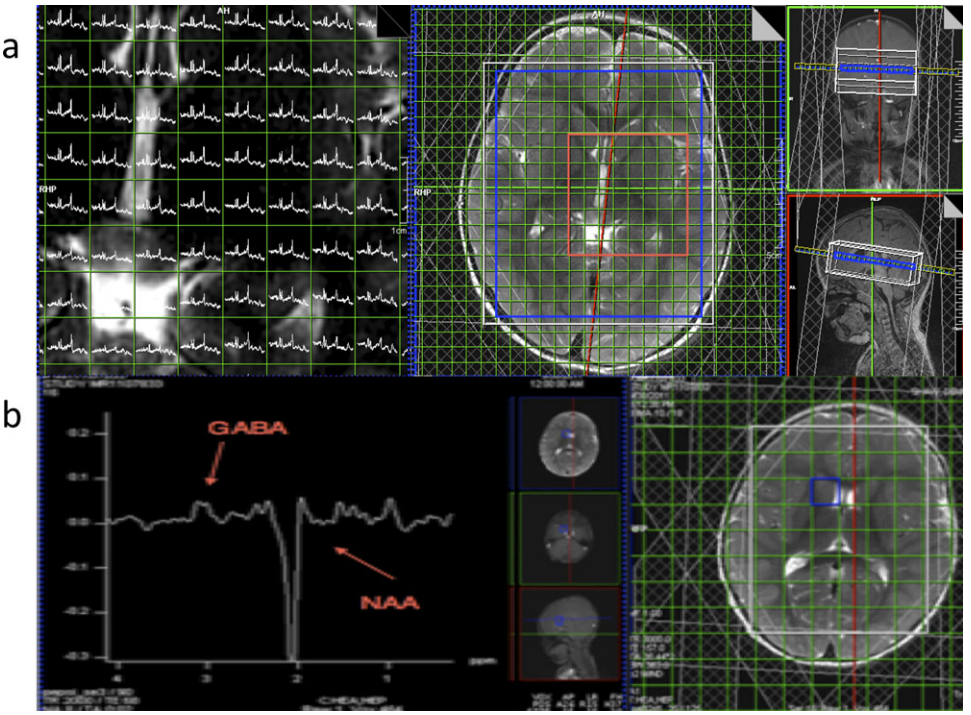

Figure 11. shows a PEPSI study at 3 Tesla in a 13-month-old infant at high-risk for Autism Spectrum Disorder. **a**: 3D short TE (15 ms) acquisition encompassing the cerebellum with voxel size = 0.34 cc acquired in 5.5 min. The 3D spectral array on the left is a subregion from a single slice, as shown in red in the middle figure, with the entire 3D volume shown on the right. **b**: GABA-edited 2-D PEPSI MRSI acquired from the cerebrum in 8.5 min with voxel size = 4 cc, showing a clearly resolved GABA peak at 3ppm. [Color figure can be viewed in the online issue, which is available at wileyonlinelibrary.com.]

taken from regions containing a significant mass of cancer cells, citrate and polyamines are significantly reduced or absent, while choline is elevated. The 3D MRSI enables efficient mapping of the entire prostate at high spatial resolution with scan times of less than 10 min using elliptical sampling (122). MRSI is usually performed with PRESS volume selection and outer volume suppression to avoid strong lipid signals from tissues around the prostate. The use of an endorectal coil is preferred over the body array for sensitivity reasons and because it immobilizes the prostate.

Applications of MRSI in the heart are challenging due to motion artifacts. ^{1}H-MRSI is particularly challenging due to poor shimming conditions and unavoidable heart movement during the long spectroscopic readout. ^{31}P-MRSI has been applied for more than two decades to measure cardiac energy metabolism (123). Applications of MRSI in muscle are

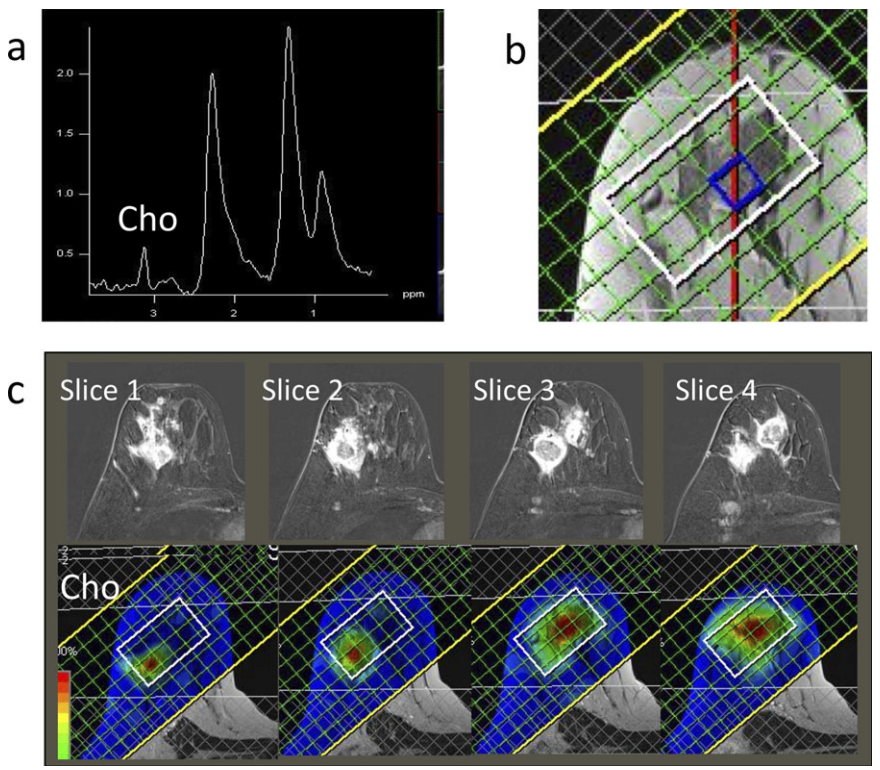

Figure 12. The 3D mapping of choline, a biomarker of breast cancer, in a patient with multifocal invasive ductal carcinoma grade 3 using PEPSI with MEGA lipid suppression and PRESS volume selection at 3 Tesla. **a**: Spectrum from the lesions in slice 4 with elevated choline and residual lipid signals. **b**: Corresponding voxel location superimposed on high resolution MRI. The white box indicates the PRESS volume selection. **c**: Dynamic contrast enhanced subtraction images and choline maps. Data acquisition parameters: TR/TE: 2 s/136 ms, matrix size: 32 × 8 × 8 voxels, voxel size: 1 cc, acquisition time including water reference scan: 10 min. [Color figure can be viewed in the online issue, which is available at wileyonlinelibrary.com.]

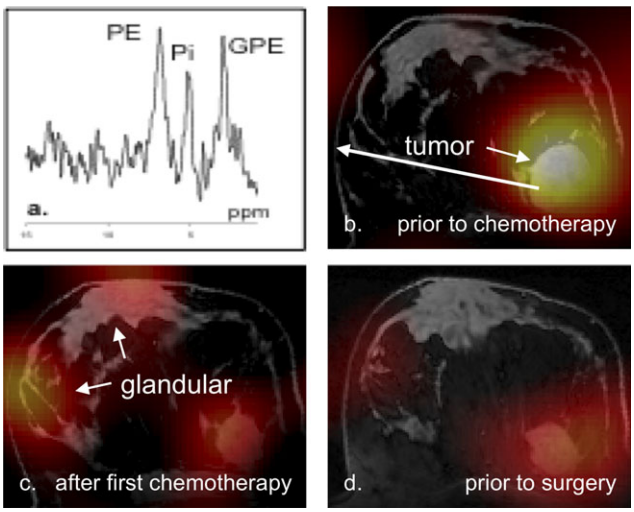

Figure 13. A ^{31}P MRSI obtained from a patient with breast cancer during chemotherapy (120). Phosphomonoesters (PE), phosphodiesters (GPE, GPC), and inorganic phosphate (Pi) can be mapped in 3D over the breast at a spatial resolution of 10 cc in an acquisition time of 20 min at 7 Tesla (**a**). The elevated PE levels in the tumor before treatment (**b**) return to similar levels as in glandular tissue (b) during chemotherapy as reflected by the colored overlay of the PE level over the lipid suppressed MRI of the human breast (b–d). Only one slice of the 3D data set is shown (Courtesy: Dr. Dennis Klomp and Dr. Vincent O. Boer - University Medical Center Utrecht, Utrecht, the Netherlands). [Color figure can be viewed in the online issue, which is available at wileyonlinelibrary.com.]

primarily aimed at mapping lipids using short TE ^{1}H-MRSI and at measuring energy metabolism using 31P MRSI. A recent study combined COSY with echo-planar encoding to improve spectral specificity by separating cross peaks arising from the skeletal muscle intramyocellular lipids and extramyocellular lipids saturated and unsaturated pools (124).

ADVANCED TOPICS

Field Strength Dependence

The SNR and spectral resolution of MRSI increase with increasing field strength. For in vivo applications using the ^{1}H nucleus, a linear gain of SNR theoretically predicted with increasing field strength (125) has been experimentally demonstrated in vivo (43,126–129). Improved spectral resolution can be observed at higher field strengths due to increased chemical shift dispersion and reduced higher-order coupling effects (130). Coupled metabolites in the human brain, such as Glu and Gln, are more easily resolved at 4 Tesla and 7 Tesla compared with 1.5 Tesla and 3Tesla (8,131,132). The spectral linewidth in ppm decreases linearly with respect to the field strength using PEPSI at 1.5, 3, 4, and 7 Tesla (43).

Increased SNR and spectral resolution in MRSI can improve the performance of metabolite quantification, or may be traded for shorter acquisition times or higher spatial resolutions. There are, however, many factors that may reduce the expected SNR and spectral resolution improvements at higher field, such as longer T_1 relaxation times that lead to saturation-related signal losses, line broadening due to magnetic susceptibility effects, shorter T_2 relaxation times that require shorter TE acquisition to maintain sensitivity, constrained RF power deposition and limitations in the design of homogeneous RF coils. Implementation of high-speed MRSI at ultra-high field (7 Tesla and beyond) is challenging due to limitations in gradient slew rate, which affects sensitivity and limits spectral width. Spatial prelocalization becomes a major challenge at high field due to increased B_1 inhomogeneity, limited B_1 amplitudes and increased specific absorption rate (SAR), which constrains RF pulse performance and elongates the minimum TE and TR compared with 3 Tesla. The increase in B_0 inhomogeneity at ultra-high field (i.e., at 7 Tesla and beyond) is a challenge for shimming that limits the sensitive volume. Some of these limitations were addressed in a recent MRSI study at 7 Tesla, which used multislice FID-based localization to minimize sensitivity losses due to limitations in RF pulse performance and SAR constraints (51). Using slice-specific B_0- and B_1-shimming to optimize spectral line width and outer volume suppression performance this study demonstrated high sensitivity and considerable improvement in spectral quality compared with previous MRSI studies at 7 Tesla (Fig. 14). Slice- and slab-specific higher-order B_0 shimming and B_1 shimming are thus expected to become indispensible for ultra-high field MRSI.

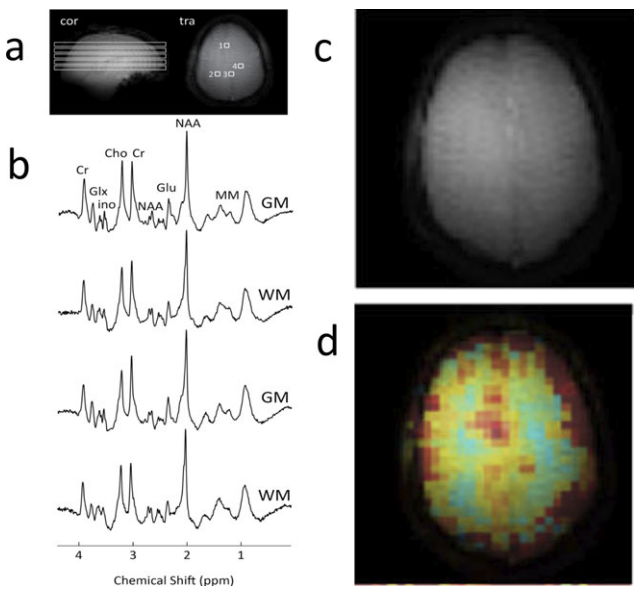

Figure 14. Multi-slice spectroscopic imaging of the human brain at 7 Tesla with an eight-element transmit coil (51). **a**: MRI with overlaid slice locations and one of the five slices with voxel locations. **b**: Corresponding spectra, where differences in the glutamate and choline and creatine ratios are apparent. In the WM the NAAG signal can be seen as a small shoulder on the right side of the NAA peak. The stable macromolecular signal indicates the high degree of lipid suppression even without in-plane volume selection and at a very short TE (2.75 ms). **c**: Supraventricular slice. **d**: Corresponding Glu/NAA map showing GM/WM contrast. Five slices with a 25 × 25 matrix were acquired in 18 min (Courtesy: Dr. Dennis Klomp and Dr. Vincent O. Boer - University Medical Center Utrecht, Utrecht, the Netherlands). [Color figure can be viewed in the online issue, which is available at wileyonlinelibrary.com.]

Ultimately, the development of RF hardware and acquisition methods that account for these limitations will be needed to more fully reap the benefits of high-field MRSI. Already, parallel transmission techniques, which combine multi-coil excitation and RF pulse design, have emerged as powerful tools to deal with B_1 inhomogeneities while controlling SAR at high field (133,134).

Coil Arrays and Parallel Imaging

The use of multiple receiver coils increases signal sensitivity and introduces additional spatial encoding capabilities, which enable image acquisition to be accelerated by reducing the number of required phase-encoding points. Parallel imaging techniques, such as simultaneous acquisition of spatial harmonics (SMASH) (135), sensitivity encoding (SENSE) (136) and generalized autocalibrating partially parallel acquisitions (GRAPPA) (137), exploit the difference in spatial sensitivity among receiver coils to reconstruct an unaliased image from regularly undersampled *k*-space data from multiple coils. Parallel imaging has been successfully applied to accelerate conventional phase-encoded MRSI (27), turbo-spin-echo MRSI (26), and PEPSI (28,29,138). Acceleration in parallel imaging is limited by noise amplification due to reduced number of phase-encoding points and instability in the inverse reconstruction produced by overlapped coil sensitivities (i.e., the so-called g-factor). Several approaches are available to decrease the SNR penalty and thus increase the acceleration capability, such as the use of high-field systems, coil arrays with large numbers of elements, and regularization of the inverse reconstruction problem. High-field systems increase the baseline SNR and reduce g-factor noise amplification due to the stronger spatial modulation of the coil reception profiles (139). The performance of parallel imaging increases with the number of coil elements, particularly for 3D imaging where multiple dimensions are available for acceleration, at least up to the g-factor limits imposed by electrodynamic constraints (140,141). Acceleration factors of 2–3 were reported for 2D MRSI using standard coil arrays with 8–12 elements (28,138), and up to 8 for 3D MRSI using a 32-element coil array (29).

The acceleration offered by parallel imaging techniques can be used to reduce total scan times and thus increase patient comfort and reduce sensitivity to motion, or can be exchanged for increased volumetric coverage and/or higher spatial resolutions depending on the available SNR. Figure 15 shows 2D metabolite concentration maps using PEPSI data acquired with acquisition times as short as 12 s using 5-fold SENSE acceleration. Parallel imaging techniques have also enabled single-shot MRSI based on the PEPSI technique, where echo-planar spatial-spectral encoding was combined with interleaved phase-encoding and SENSE reconstruction to perform 2D metabolic mapping within a single excitation (30).

The increased encoding capabilities of many-element coil arrays have enabled the use of alternative *k*-space undersampling patterns that are not feasible with standard few-element coil arrays. MRSI using a single phase-encoding step was proposed in the inverse-PEPSI technique by performing an image reconstruction similar to that in magnetoencephalography (MEG) (142). The price to pay for these extreme levels of acceleration is reconstruction with low spatial resolution as dictated by the degree of variation of the coil sensitivity maps. An intermediate approach between standard parallel imaging and inverse imaging was presented in the superresolution SENSE (SURE-SENSE) method (140,141,143), where intravoxel coil sensitivity variations were exploited to increase the spatial resolution of low-resolution acquisitions. Acquiring a low-resolution image instead of a single phase-encoding point reduces the severe ill-conditioning in the inverse imaging method and reconstruction with higher spatial resolution is feasible with SURE-SENSE at the expense of decreasing the high acceleration factor. SURE-SENSE enables acceleration along the readout dimension for echo-planar trajectories, which is not feasible with standard parallel imaging techniques, and it is particularly useful for reducing lipid contamination, which is one of the main challenges in short-TE MRSI.

Compressed Sensing

In vivo MRSI data are characterized by limited spectral information, which is in part due to line broadening and signal relaxation. For example, long TE data and hyperpolarized MRSI data contain only a small number of spectral components that can be described with few parameters. Such spectra are called *sparse* and can be acquired with fewer data points than traditional methods using under-sampled acquisition and reconstruction methods such as *compressed sensing*. Compressed sensing is a recently developed fast imaging method that exploits sparsity of medical images to reconstruct under-sampled data (144). Instead of acquiring the fully-sampled image and compressing it afterward (standard compression), compressed sensing applies the fact than an image is usually sparse under an appropriate basis and reconstructs this sparse representation from undersampled data. The number of required samples in practice is approximately 3–5 times the number of sparse coefficients, which represents a substantial acceleration if the number of sparse coefficients is much less than the total number of points (144). The same principle can be applied in the spectral domain.

^{13}C-MRSI is a promising technique for testing different metabolic pathways to study normal metabolism and characterize disease physiology (145). However, ^{13}C-MRSI suffers in a particularly acute manner from low signal sensitivity, resulting in long acquisition times due to the need to perform averaging, and large voxel sizes to obtain spectra with adequate SNR. The use of hyperpolarized compounds has been demonstrated to boost signal sensitivity for ^{13}C-MRSI (146). For example, SNR gains of over 40,000 were demonstrated for [1-13C]-pyruvate. However, highly accelerated acquisitions are required to measure metabolic information during the short decay period of enhanced polarization, which is on the order of tens of seconds. One powerful constraint that can be exploited to

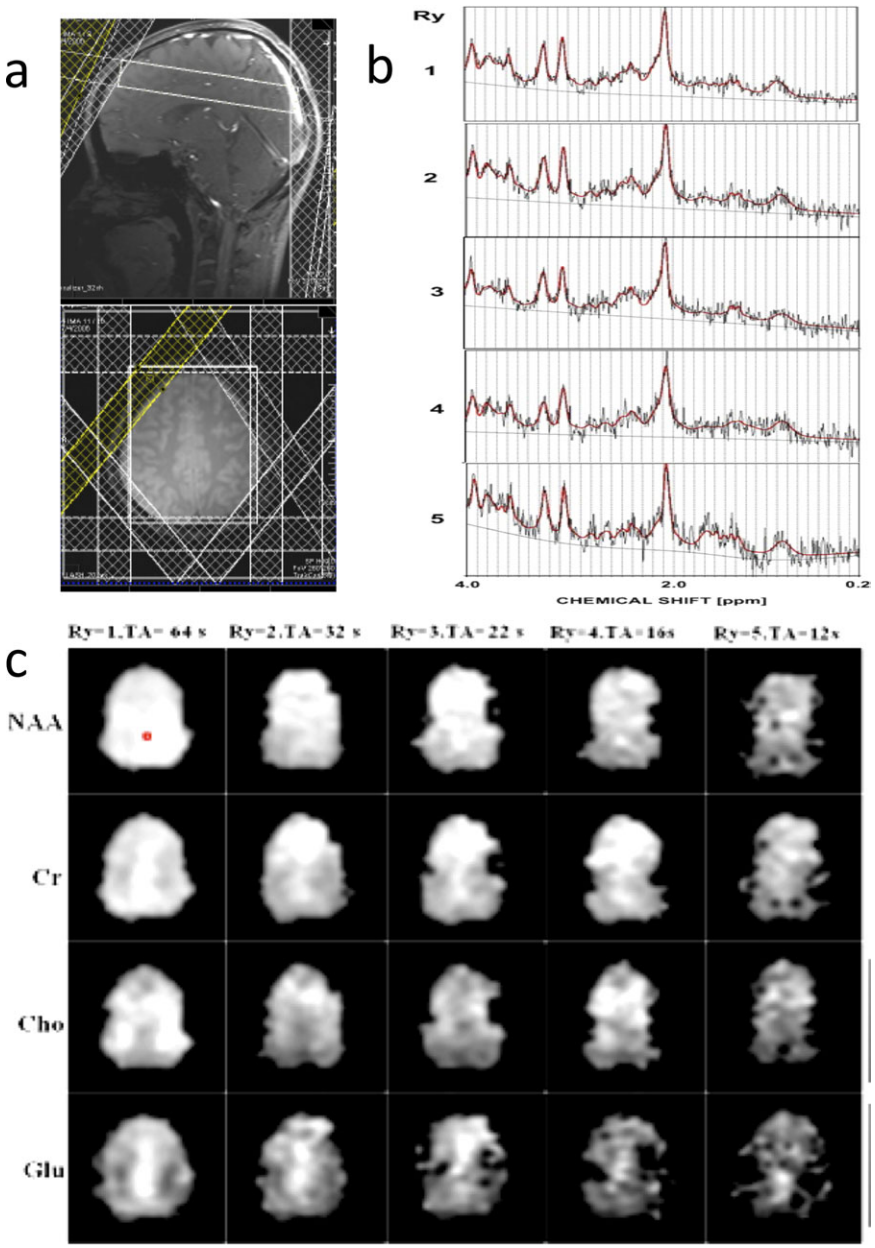

Figure 15. Simulated SENSE acceleration of 2D PEPSI data acquired at 3 Tesla using a 32-channel array. **a**: Slice localization. **b**: Spectra with LCModel fit from central gray matter with up to 5-fold acceleration (R_y), which corresponds to an effective acquisition time of 12 s. **c**: Metabolite maps of Choline, Creatine and Glutamate with up to 5-fold acceleration. Acquisition parameters: TE: 15 ms, TR: 2 s, 32 × 32 matrix, voxel size: 1.1 cc, acquisition time: 64 s. [Color figure can be viewed in the online issue, which is available at wileyonlinelibrary.com.]

further accelerate data acquisition is the sparsity of ^{13}C spectra. Compressed sensing was applied to increase the spatial resolution of ^{13}C-MRSI data using an echo-planar trajectory with random sampling along the phase-encoding dimensions (15,147).

The application of compressed sensing in MRSI is not limited to ^{13}C and can also be used to accelerate ^{1}H-MRSI, given an appropriate sparsifying transform and randomized undersampling pattern to generate the required incoherent aliasing artifacts. Moreover, compressed sensing can be combined with other acceleration techniques to further increase the acceleration rate. For example, the combination of compressed sensing and parallel imaging was demonstrated to provide higher acceleration rates for PEPSI (31), which in turn can be exploited to enable previously not possible combinations of total scan time, volumetric coverage and spatial resolution.

CONCLUSIONS

MRSI has benefitted from the rapid development of clinical MRI technology that introduced techniques such as prospective motion correction, higher-order dynamic B_0 shimming, B_1-shimming, parallel imaging with large scale array coils and compressed sensing, all of which have been or are in the process of being adapted for MRSI. High-speed MRSI in combination with high field strengths and sensitive array RF coils now enable shorter acquisition times and increased spatial resolution, along with improved anatomical coverage compared with conventional phase-encoded MRSI methods. Conventional phase-encoded MRSI will continue to be the standard for clinical MRSI for some time, but it is restricted to applications in which limited volume coverage or low spatial resolution are acceptable.

High-speed ^{1}H-MRSI is well suited to replace conventional ^{1}H-MRSI in the brain where acceptable magnetic field homogeneity can be achieved and large volume coverage and high spatial resolution are desirable. Echo-planar based techniques enable 3D mapping with whole brain coverage in scan time on the order of 15 min, and partial brain coverage in scan times of less than 10 min. Combining high-speed MRSI with parallel imaging enables whole brain coverage with scan times of less than 10 min. Integration of recently developed motion and dynamic shim correction methods is desirable to reduce motion artifacts that are often underestimated in clinical MRSI. Fully automated and reproducible setup of MRSI volume selection and outer volume suppression slices is now feasible for brain MRSI studies and adaptation for other organs should be explored. Further improvements of the performance of outer volume suppression RF pulses for application in the brain are required to achieve consistent lipid suppression in peripheral areas and to enable short TE acquisition, which is desirable at high field to maximize sensitivity. It is also desirable to automatically reconstruct and quantify spectroscopic images on the scanner immediately after the scan to enable online quality control and to facilitate integration into clinical routine.

MRSI can be used at any field strength, but the linear increase in sensitivity with field strength favors the highest field strength that is suitable for clinical studies. The 3 Tesla scanners, which are widely available and technologically mature, are currently the preferred platform for MRSI. 4 Tesla and 4.7 Tesla are field strengths that offer substantial gains in sensitivity compared with 3 Tesla, they are quite compatible with the current state-of-the-art in clinical hardware, and B_1-inhomogeneity is moderate, but the clinical manufacturers unfortunately do not support these field strengths. 7 Tesla scanners are developing rapidly to overcome the technical challenges of B_0 and B_1 inhomogeneity and gradient performance limitations. It is expected that volumetric mapping of J-coupled metabolites in the brain with improved spatial resolution comparable to that of PET scanning in clinically acceptable measurement times will become feasible. These advances have the potential to significantly change the clinical impact of MRSI and stimulate novel research applications.

Most ^{1}H-MRSI studies in the brain focus on quantification of myo-Inositol, Cho, Cr, and NAA (and Lac), which are the most easily measured brain metabolites. In the future, it is anticipated that a much wider range of J-coupled metabolites will be robustly measured, such as GABA, Glutamate, and Glutamine, reflecting the continuing improvements in scanner hardware technology at high field strength. Novel metabolic contrasts available with hyperpolarized MRI that enable real-time mapping of enzymatic reaction rates will have considerable impact on future applications of MRSI and technology development. We anticipate that while spectral quantification will remain an important goal for clinical MRSI, increases in spatial resolution approaching that of fMRI and coregistration with anatomical MRI will have considerable impact on clinical acceptance. Single voxel spectroscopy will remain an important tool for measuring metabolites that are not detectable with MRSI for sensitivity reasons and for measurements in regions where magnetic field inhomogeneity degrades spectral quality in MRSI.

MRSI has been most successful for characterizing brain diseases. The strong metabolic changes in brain tumors and multiple sclerosis are striking examples of MRSI applications, which are useful for guiding therapy (e.g., presurgical mapping or chemotherapy). Studies of psychiatric disease are perhaps the most challenging applications of MRSI, because they require extremely stable and reproducible measurements of minute changes in metabolite concentration. It is also important to remember that MRSI should not be seen in isolation, but as part of a multi-modal imaging approach that maximizes information per unit time. As such, an MRSI protocol is complementary to other molecular imaging techniques, including PET.

However, barriers remain that hamper the acceptance of MRSI as a clinical modality. For example, the wide range of MRSI techniques that are used for clinical applications, which makes comparisons between studies difficult and reflects a situation that is similar to the early days of single voxel MRS. Consensus regarding the preferred encoding and prelocalization methods is only slowly emerging. There is a lack of standardization of quantification methods, which is not uncharacteristic for a methodology that relies heavily on modeling and on a priori information. More generally, MRSI is technically challenging in most clinical settings and requires special training, which limits widespread acceptance. For some time these perceived limitations and the perceived lack of innovative ideas to move the field forward have impacted federal funding in the US for MRSI method development and clinical applications, and discouraged young scientist to make a career in MRSI. Increased standardization facilitated by the technical advances described above will encourage large-scale controlled studies to document the clinical impact of MRSI on diagnosis and treatment outcome, requisite for MRSI becoming reimbursable by major insurance carriers.

ACKNOWLEDGMENT

We gratefully acknowledge the contributions of our colleagues, and former and present team members who participated in the development and application of high-speed MRSI: Elena Ackley, Dr. Patrick Bolan, Dr. Linda Casey, Dr. Muhammad Omar Chohan, Dr. Zoneddy Dayao, Dr. Ulrike Dydak, Dr. Stephen Eberhardt, Dr. Bruce Fisch, Dr. Pierre-Gilles Henry, Dr. Sang-Joon Lee, Dr. Fa-Hsuan Lin, Dr. Lesley Lomo, Susan Lopez, Dr. Malgorzata Marjanska, Dr. Manel Martinez Ramon, Dr. Ashwani Rajput, Dr. Melanie Royce, Dr. John Russell, Dr. Laurel Sillerud, Dr. Shang-Yueh Tsai, Dr. Jun S. Xu, Dr. Howard Yonas, Akio Yoshimoto, Dr. Guang Di Yung, Dr. Chenguang Zhao, Dr. Tongsheng Zhang, and Dr. Weili Zheng. We thank Dr. Andrew Maudsley and Dr. Mohammed Sabati from the Department of

Radiology, Miller School of Medicine University of Miami, FL, and Dr. Dennis Klomp and Dr. Vincent O. Boer from the University Medical Center Utrecht, Utrecht, the Netherlands for contributing figures and sharing preliminary results.

REFERENCES

1. Brown TR, Kincaid BM, Ugurbil K. NMR chemical shift imaging in three dimensions. Proc Natl Acad Sci U S A 1982;79: 3523–3526.
2. Maudsley AA, Hilal SK, Perman WH, Simon HE. Spatially resolved high resolution spectroscopy by "four-dimensional" NMR. J Magn Reson (1969) 1983;51:147–152.
3. Alger JR. Quantitative proton magnetic resonance spectroscopy and spectroscopic imaging of the brain: a didactic review. Top Magn Reson Imaging 2011;21:115–128.
4. Yung KT, Zheng W, Zhao C, Martinez-Ramon M, van der Kouwe A, Posse S. Atlas-based automated positioning of outer volume suppression slices in short-echo time 3D MR spectroscopic imaging of the human brain. Magn Reson Med 2011;66: 911–922.
5. Maudsley AA, Domenig C, Sheriff S. Reproducibility of serial whole-brain MR spectroscopic imaging. NMR Biomed 2010;23: 251–256.
6. Noworolski SM, Nelson SJ, Henry RG, et al. High spatial resolution 1H-MRSI and segmented MRI of cortical gray matter and subcortical white matter in three regions of the human brain. Magn Reson Med 1999;41:21–29.
7. Bydder GM, Young IR. MR imaging: clinical use of the inversion recovery sequence. J Comput Assist Tomogr 1985;9:659–675.
8. Posse S, Otazo R, Caprihan A, et al. Proton echo-planar spectroscopic imaging of J-coupled resonances in human brain at 3 and 4 Tesla. Magn Reson Med 2007;58:236–244.
9. Edelstein WA, Hutchison JM, Johnson G, Redpath T. Spin warp NMR imaging and applications to human whole-body imaging. Phys Med Biol 1980;25:751–756.
10. Posse S. Direct imaging of magnetic field gradients by group spin-echo selection. Magn Reson Med 1992;25:12–29.
11. Mayer D, Dreher W, Leibfritz D. Fast echo planar based correlation-peak imaging: demonstration on the rat brain in vivo. Magn Reson Med 2000;44:23–28.
12. Srinivasan R, Cunningham C, Chen A, et al. TE-averaged two-dimensional proton spectroscopic imaging of glutamate at 3 T. Neuroimage 2006;30:1171–1178.
13. Dydak U, Xu JS, Marjanska M, Posse S. 3D GABA spectroscopic imaging using MEGA-PEPSI. In: Proceedings of the 19th Annual Meeting of ISMRM, Montreal, Canada, 2011. (abstract 1428).
14. Mayer D, Levin YS, Hurd RE, Glover GH, Spielman DM. Fast metabolic imaging of systems with sparse spectra: application for hyperpolarized 13C imaging. Magn Reson Med 2006;56: 932–937.
15. Hu S, Lustig M, Chen AP, et al. Compressed sensing for resolution enhancement of hyperpolarized 13C flyback 3D-MRSI. J Magn Reson 2008;192:258–264.
16. Mansfield P. Spatial mapping of the chemical shift in NMR. Magn Reson Med 1984;1:370–386.
17. Webb P, Spielman D, Macovski A. A fast spectroscopic imaging method using a blipped phase encode gradient. Magn Reson Med 1989;12:306–315.
18. Posse S, DeCarli C, Le Bihan D. Three-dimensional echo-planar MR spectroscopic imaging at short echo times in the human brain. Radiology 1994;192:733–738.
19. Posse S, Tedeschi G, Risinger R, Ogg R, Lebihan D. High-speed H-1 spectroscopic imaging in human brain by echo-planar spatial-spectral encoding. Magn Reson Med 1995;33:34–40.
20. Metzger G, Hu XP. Application of interlaced Fourier transform to echo-planar spectroscopic imaging. J Magn Reson 1997;125: 166–170.
21. Adalsteinsson E, Irarrazabal P, Topp S, Meyer C, Macovski A, Spielman DM. Volumetric spectroscopic imaging with spiral-based k-space trajectories. Magn Reson Med 1998;39:889–898.
22. Dixon WT. Simple proton spectroscopic imaging. Radiology 1984;153:189–194.
23. Guimaraes AR, Baker JR, Jenkins BG, et al. Echoplanar chemical shift imaging. Magn Reson Med 1999;41:877–882.
24. Norris DG, Dreher W. Fast proton spectroscopic imaging using the sliced k-space method. Magn Reson Med 1993;30:641–645.
25. Duyn JH, Moonen CT. Fast proton spectroscopic imaging of human brain using multiple spin-echoes. Magn Reson Med 1993;30:409–414.
26. Dydak U, Pruessmann KP, Weiger M, Tsao J, Meier D, Boesiger P. Parallel spectroscopic imaging with spin-echo trains. Magn Reson Med 2003;50:196–200.
27. Dydak U, Weiger M, Pruessmann KP, Meier D, Boesiger P. Sensitivity-encoded spectroscopic imaging. Magn Reson Med 2001; 46:713–722.
28. Lin FH, Tsai SY, Otazo R, et al. Sensitivity-encoded (SENSE) proton echo-planar spectroscopic imaging (PEPSI) in the human brain. Magn Reson Med 2007;57:249–257.
29. Otazo R, Tsai SY, Lin FH, Posse S. Accelerated short-TE 3D proton echo-planar spectroscopic imaging using 2D-SENSE with a 32-channel array coil. Magn Reson Med 2007;58:1107–1116.
30. Posse S, Otazo R, Tsai SY, Yoshimoto AE, Lin FH. Single-shot magnetic resonance spectroscopic imaging with partial parallel imaging. Magn Reson Med 2009;61:541–547.
31. Otazo R, Sodickson D, Yoshimoto A, Posse S. Accelerated proton echo-planar spectroscopic imaging using parallel imaging and compressed sensing. In: Proceedings of the 18th Annual Meeting of ISMRM, Honolulu, Hawaii, 2009. (abstract 331).
32. Dreher W, Geppert C, Althaus M, Leibfritz D. Fast proton spectroscopic imaging using steady-state free precession methods. Magn Reson Med 2003;50:453–460.
33. Schuster C, Dreher W, Geppert C, Leibfritz D. Fast 3D 1H spectroscopic imaging at 3 Tesla using spectroscopic missing-pulse SSFP with 3D spatial preselection. Magn Reson Med 2007;57: 82–89.
34. Dreher W, Erhard P, Leibfritz D. Fast three-dimensional proton spectroscopic imaging of the human brain at 3 T by combining spectroscopic missing pulse steady-state free precession and echo planar spectroscopic imaging. Magn Reson Med 2011;66: 1518–1525.
35. Hu X, Levin DN, Lauterbur PC, Spraggins T. SLIM: spectral localization by imaging. Magn Reson Med 1988;8:314–322.
36. Goelman G, Subramanian VH, Leigh JS. Transverse Hadamard spectroscopic imaging technique. J Magn Reson (1969) 1990; 89:437–454.
37. Gonen O, Hu J, Stoyanova R, Leigh JS, Goelman G, Brown TR. Hybrid three dimensional (1D-Hadamard, 2D-chemical shift imaging) phosphorus localized spectroscopy of phantom and human brain. Magn Reson Med 1995;33:300–308.
38. Pohmann R, von Kienlin M, Haase A. Theoretical evaluation and comparison of fast chemical shift imaging methods. J Magn Reson 1997;129:145–160.
39. Posse S, Dager SR, Richards TL, et al. In vivo measurement of regional brain metabolic response to hyperventilation using magnetic resonance: proton echo planar spectroscopic imaging (PEPSI). Magn Reson Med 1997;37:858–865.
40. Hanson LG, Schaumburg K, Paulson OB. Reconstruction strategy for echo planar spectroscopy and its application to partially undersampled imaging. Magn Reson Med 2000;44:412–417.
41. Cunningham CH, Vigneron DB, Chen AP, et al. Design of flyback echo-planar readout gradients for magnetic resonance spectroscopic imaging. Magn Reson Med 2005;54:1286–1289.
42. Ebel A, Maudsley AA. Detection and correction of frequency instabilities for volumetric 1H echo-planar spectroscopic imaging. Magn Reson Med 2005;53:465–469.
43. Otazo R, Mueller B, Ugurbil K, Wald L, Posse S. Signal-to-noise ratio and spectral linewidth improvements between 1.5 and 7 Tesla in proton echo-planar spectroscopic imaging. Magn Reson Med 2006;56:1200–1210.
44. Ordidge RJ, Bendall MR, Gordon RE, Connelly A. Volume selection for invivo biological spectroscopy. In: Govil G, Khetrapal CL, Saran A, editors. Magnetic resonance in biology and medicine. New Delhi: Tata McGraw-Hill Publishing Company Ltd; 1985. p 387–397.
45. Frahm J, Merboldt K-D, Hanicke W. Localized proton spectroscopy using stimulated echoes. J Magn Reson (1969) 1987;72: 502–508.

46. McNab JA, Bartha R. Quantitative short echo-time 1H LASER-CSI in human brain at 4 T. NMR Biomed 2006;19:999–1009.
47. Scheenen TW, Klomp DW, Wijnen JP, Heerschap A. Short echo time 1H-MRSI of the human brain at 3T with minimal chemical shift displacement errors using adiabatic refocusing pulses. Magn Reson Med 2008;59:1–6.
48. Duyn JH, Gillen J, Sobering G, Vanzijl PCM, Moonen CTW. Multisection proton MR spectroscopic imaging of the brain. Radiology 1993;188:277–282.
49. Ebel A, Maudsley AA. Improved spectral quality for 3D MR spectroscopic imaging using a high spatial resolution acquisition strategy. Magn Reson Imaging 2003;21:113–120.
50. Mathiesen HK, Tscherning T, Sorensen PS, et al. Multi-slice echo-planar spectroscopic MR imaging provides both global and local metabolite measures in multiple sclerosis. Magn Reson Med 2005;53:750–759.
51. Boer VO, Klomp DW, Juchem C, Luijten PR, de Graaf RA. Multislice (1) H MRSI of the human brain at 7 T using dynamic B(0) and B(1) shimming. Magn Reson Med 2012;68:662–670.
52. Singh S, Rutt BK, Henkelman RM. Projection presaturation - a fast and accurate technique for multidimensional spatial localization. J Magn Reson 1990;87:567–583.
53. Singh S, Rutt BK, Napel S. Projection presaturation. 2. Single-shot localization of multiple regions of interest. J Magn Reson 1990;90:313–329.
54. Singh S, Brody WR. Projection presaturation. 3. Accurate selective excitation or presaturation of the regions of tailored shape in the presence of short-T(1) species. J Magn Reson Ser B 1993; 101:52–62.
55. Duijn JH, Matson GB, Maudsley AA, Weiner MW. 3D phase encoding 1H spectroscopic imaging of human brain. Magn Reson Imaging 1992;10:315–319.
56. Posse S, Schuknecht B, Smith ME, van Zijl PC, Herschkowitz N, Moonen CT. Short echo time proton MR spectroscopic imaging. J Comput Assist Tomogr 1993;17:1–14.
57. Provencher SW. Estimation of metabolite concentrations from localized in vivo proton NMR-spectra. Magn Reson Med 1993; 30:672–679.
58. Chu A, Alger JR, Moore GJ, Posse S. Proton echo-planar spectroscopic imaging with highly effective outer volume suppression using combined presaturation and spatially selective echo dephasing. Magn Reson Med 2003;49:817–821.
59. Tran TK, Vigneron DB, Sailasuta N, et al. Very selective suppression pulses for clinical MRSI studies of brain and prostate cancer. Magn Reson Med 2000;43:23–33.
60. Henning A, Fuchs A, Murdoch JB, Boesiger P. Slice-selective FID acquisition, localized by outer volume suppression (FIDLOVS) for (1)H-MRSI of the human brain at 7 T with minimal signal loss. NMR Biomed 2009;22:683–696.
61. Henning A, Schar M, Schulte RF, Wilm B, Pruessmann KP, Boesiger P. SELOVS: brain MRSI localization based on highly selective T1- and B1- insensitive outer-volume suppression at 3T. Magn Reson Med 2008;59:40–51.
62. Venugopal N, McCurdy B, Hovdebo J, et al. Automatic conformal prescription of very selective saturation bands for in vivo (1) H-MRSI of the prostate. NMR Biomed 2012;25:643–653.
63. Ozhinsky E, Vigneron DB, Nelson SJ. Improved spatial coverage for brain 3D PRESS MRSI by automatic placement of outer-volume suppression saturation bands. J Magn Reson Imaging 2011;33:792–802.
64. Martinez-Ramon M, Gallardo-Antolin A, Cid-Sueiro J, et al. Automatic placement of outer volume suppression slices in MR spectroscopic imaging of the human brain. Magn Reson Med 2010;63:592–600.
65. van der Kouwe AJ, Benner T, Fischl B, et al. On-line automatic slice positioning for brain MR imaging. Neuroimage 2005;27: 222–230.
66. Benner T, Wisco JJ, van der Kouwe AJ, et al. Comparison of manual and automatic section positioning of brain MR images. Radiology 2006;239:246–254.
67. Bornert P, Schaffter T. Curved slice imaging. Magn Reson Med 1996;36:932–939.
68. Maudsley AA, Domenig C, Govind V, et al. Mapping of brain metabolite distributions by volumetric proton MR spectroscopic imaging (MRSI). Magn Reson Med 2009;61:548–559.
69. Balchandani P, Spielman D. Fat suppression for 1H MRSI at 7T using spectrally selective adiabatic inversion recovery. Magn Reson Med 2008;59:980–988.
70. Star-Lack J, Nelson SJ, Kurhanewicz J, Huang LR, Vigneron DB. Improved water and lipid suppression for 3D PRESS CSI using RF band selective inversion with gradient dephasing (BASING). Magn Reson Med 1997;38:311–321.
71. Ogg RJ, Kingsley PB, Taylor JS. WET, a T1- and B1-insensitive water-suppression method for in vivo localized 1H NMR spectroscopy. J Magn Reson B 1994;104:1–10.
72. Tkac I, Starcuk Z, Choi IY, Gruetter R. In vivo 1H NMR spectroscopy of rat brain at 1 ms echo time. Magn Reson Med 1999;41: 649–656.
73. Spielman D, Meyer C, Macovski A, Enzmann D. H-1 Spectroscopic Imaging Using a Spectral Spatial Excitation Pulse. Magn Reson Med 1991;18:269–279.
74. Hurd RE, Gurr D, Sailasuta N. Proton spectroscopy without water suppression: the oversampled J-resolved experiment. Magn Reson Med 1998;40:343–347.
75. Dong Z, Dreher W, Leibfritz D. Experimental method to eliminate frequency modulation sidebands in localized in vivo 1H MR spectra acquired without water suppression. Magn Reson Med 2004;51:602–606.
76. Dong Z, Dreher W, Leibfritz D. Toward quantitative short-echo-time in vivo proton MR spectroscopy without water suppression. Magn Reson Med 2006;55:1441–1446.
77. Mandal PK. In vivo proton magnetic resonance spectroscopic signal processing for the absolute quantitation of brain metabolites. Eur J Radiol 2012;81:e653–e664.
78. Weber-Fahr W, Ende G, Braus DF, et al. A fully automated method for tissue segmentation and CSF-correction of proton MRSI metabolites corroborates abnormal hippocampal NAA in schizophrenia. Neuroimage 2002;16:49–60.
79. Maudsley AA, Darkazanli A, Alger JR, et al. Comprehensive processing, display and analysis for in vivo MR spectroscopic imaging. NMR Biomed 2006;19:492–503.
80. Dong Z, Peterson B. The rapid and automatic combination of proton MRSI data using multi-channel coils without water suppression. Magn Reson Imaging 2007;25:1148–1154.
81. Maril N, Lenkinski RE. An automated algorithm for combining multivoxel MRS data acquired with phased-array coils. J Magn Reson Imaging 2005;21:317–322.
82. Rodgers CT, Robson MD. Receive array magnetic resonance spectroscopy: whitened singular value decomposition (WSVD) gives optimal Bayesian solution. Magn Reson Med 2010;63: 881–891.
83. Brown MA. Time-domain combination of MR spectroscopy data acquired using phased-array coils. Magn Reson Med 2004;52: 1207–1213.
84. Gasparovic C, Song T, Devier D, et al. Use of tissue water as a concentration reference for proton spectroscopic imaging. Magn Reson Med 2006;55:1219–1226.
85. Kreis R, Slotboom J, Hofmann L, Boesch C. Integrated data acquisition and processing to determine metabolite contents, relaxation times, and macromolecule baseline in single examinations of individual subjects. Magn Reson Med 2005;54: 761–768.
86. Liu S, Fleysher R, Fleysher L, et al. Brain metabolites B1-corrected proton T1 mapping in the rhesus macaque at 3 T. Magn Reson Med 2010;63:865–871.
87. Tsai SY, Posse S, Lin YR, et al. Fast mapping of the T2 relaxation time of cerebral metabolites using proton echo-planar spectroscopic imaging (PEPSI). Magn Reson Med 2007;57:859–865.
88. Bagory M, Durand-Dubief F, Ibarrola D, Confavreux C, Sappey-Marinier D. "Absolute" quantification in magnetic resonance spectroscopy: validation of a clinical protocol in multiple sclerosis. Conf Proc IEEE Eng Med Biol Soc 2007;2007:3458–3461.
89. Ebel A, Soher BJ, Maudsley AA. Assessment of 3D proton MR echo-planar spectroscopic imaging using automated spectral analysis. Magn Reson Med 2001;46:1072–1078.
90. Hofmann L, Slotboom J, Jung B, Maloca P, Boesch C, Kreis R. Quantitative 1H-magnetic resonance spectroscopy of human brain: influence of composition and parameterization of the basis set in linear combination model-fitting. Magn Reson Med 2002;48:440–453.

91. Laudadio T, Selen Y, Vanhamme L, Stoica P, Van Hecke P, Van Huffel S. Subspace-based MRS data quantitation of multiplets using prior knowledge. J Magn Reson 2004;168:53–65.
92. Provencher SW. Estimation of metabolite concentrations from localized in vivo proton NMR spectra. Magn Reson Med 1993; 30:672–679.
93. Provencher SW. Automatic quantitation of localized in vivo 1H spectra with LCModel. NMR Biomed 2001;14:260–264.
94. Ratiney H, Sdika M, Coenradie Y, Cavassila S, van Ormondt D, Graveron-Demilly D. Time-domain semi-parametric estimation based on a metabolite basis set. NMR Biomed 2005;18:1–13.
95. Vanhamme L, Van Huffel S, Van Hecke P, van Ormondt D. Time-domain quantification of series of biomedical magnetic resonance spectroscopy signals. J Magn Reson 1999;140: 120–130.
96. Gillies P, Marshall I, Asplund M, Winkler P, Higinbotham J. Quantification of MRS data in the frequency domain using a wavelet filter, an approximated Voigt lineshape model and prior knowledge. NMR Biomed 2006;19:617–626.
97. Mierisova S, Ala-Korpela M. MR spectroscopy quantitation: a review of frequency domain methods. NMR Biomed 2001;14: 247–259.
98. Naressi A, Couturier C, Devos JM, et al. Java-based graphical user interface for the MRUI quantitation package. MAGMA 2001;12:141–152.
99. Slotboom J, Boesch C, Kreis R. Versatile frequency domain fitting using time domain models and prior knowledge. Magn Reson Med 1998;39:899–911.
100. Corrigan NM, Richards TL, Friedman SD, Petropoulos H, Dager SR. Improving 1H MRSI measurement of cerebral lactate for clinical applications. Psychiatry Res 2010;182:40–47.
101. Maudsley AA, Darkazanli A, Alger JR, et al. Comprehensive processing, display and analysis for in vivo MR spectroscopic imaging. NMR Biomed 2006;19:492–503.
102. Posse S, Cuenod CA, Lebihan D. Motion artifact compensation in H-1 spectroscopic imaging by signal tracking. J Magn Reson Ser B 1993;102:222–227.
103. Lin JM, Tsai SY, Liu HS, et al. Quantification of non-water-suppressed MR spectra with correction for motion-induced signal reduction. Magn Reson Med 2009;62:1394–1403.
104. Hess AT, Andronesi OC, Tisdall MD, Sorensen AG, van der Kouwe AJ, Meintjes EM. Real-time motion and B0 correction for localized adiabatic selective refocusing (LASER) MRSI using echo planar imaging volumetric navigators. NMR Biomed 2012; 25:347–358.
105. Mason GF, Pan JW, Ponder SL, Twieg DB, Pohost GM, Hetherington HP. Detection of brain glutamate and glutamine in spectroscopic images at 4.1 T. Magn Reson Med 1994;32:142–145.
106. Pan JW, Mason GF, Pohost GM, Hetherington HP. Spectroscopic imaging of human brain glutamate by water-suppressed J-refocused coherence transfer at 4.1 T. Magn Reson Med 1996;36: 7–12.
107. Yung K, Tsai SY, Lin FH, Henry PG, Yoshimoto A, Posse S. Comparison of TE-averaged with short TE Proton-Echo-Planar-Spectroscopic-Imaging (PEPSI) for mapping glutamate in human brain at 3T. In: Proceedings of the 18th Annual Meeting of ISMRM, Honolulu, Hawaii, 2009. (abstract 4314).
108. Shen J, Shungu DC, Rothman DL. In vivo chemical shift imaging of gamma-aminobutyric acid in the human brain. Magn Reson Med 1999;41:35–42.
109. Jensen JE, Frederick BD, Wang L, Brown J, Renshaw PF. Two-dimensional, J-resolved spectroscopic imaging of GABA at 4 Tesla in the human brain. Magn Reson Med 2005;54:783–788.
110. Zhu H, Edden RA, Ouwerkerk R, Barker PB. High resolution spectroscopic imaging of GABA at 3 Tesla. Magn Reson Med 2011;65:603–609.
111. Dager SR, Layton ME, Strauss W, et al. Human brain metabolic response to caffeine and the effects of tolerance. Am J Psychiatry 1999;156:229–237.
112. Dager SR, Corrigan NM, Richards TL, Posse S. Research applications of magnetic resonance spectroscopy to investigate psychiatric disorders. Top Magn Reson Imaging 2008;19:81–96.
113. Kuehn BM. CDC: autism spectrum disorders common. JAMA 2007;297:940.
114. Friedman SD, Shaw DW, Artru AA, et al. Regional brain chemical alterations in young children with autism spectrum disorder. Neurology 2003;60:100–107.
115. Friedman SD, Shaw DW, Artru AA, Dawson G, Petropoulos H, Dager SR. Gray and white matter brain chemistry in young children with autism. Arch Gen Psychiatry 2006;63:786–794.
116. Dager S, Corrigan, NM, Richards, TL, Shaw, DWW. Autism spectrum disorders. In: Amaral D, Geshwind D, Dawson G, editors. Brain chemistry: magnetic resonance spectroscopy. Cambridge: Oxford University Press; 2011. p 576–592.
117. Huang W, Fisher PR, Dulaimy K, Tudorica LA, O'Hea B, Button TM. Detection of breast malignancy: diagnostic MR protocol for improved specificity. Radiology 2004;232:585–591.
118. Danishad KK, Sharma U, Sah RG, Seenu V, Parshad R, Jagannathan NR. Assessment of therapeutic response of locally advanced breast cancer (LABC) patients undergoing neoadjuvant chemotherapy (NACT) monitored using sequential magnetic resonance spectroscopic imaging (MRSI). NMR Biomed 2010;23: 233–241.
119. Zhao C, Bolan P, Royce M, Lakkadi L, Lee S-J, Eberhardt S, Posse S. High-speed MR spectroscopic imaging of total choline in breast cancer and healthy controls at 3T: a feasibility study. In: Proceedings of the 19th Annual Meeting of ISMRM, Montreal, Canada. 2011. (abstract 513).
120. Klomp DW, van de Bank BL, Raaijmakers A, et al. (31) P MRSI and (1) H MRS at 7 T: initial results in human breast cancer. NMR Biomed 2011;24:1337–1342.
121. Kurhanewicz J, Vigneron DB. Advances in MR spectroscopy of the prostate. Magn Reson Imaging Clin N Am 2008;16:697–710, ix-x.
122. Verma S, Rajesh A, Futterer JJ, et al. Prostate MRI and 3D MR spectroscopy: how we do it. AJR Am J Roentgenol 2010;194: 1414–1426.
123. Meyerhoff DJ, Maudsley AA, Schaefer S, Weiner MW. Phosphorus-31 magnetic resonance metabolite imaging in the human body. Magn Reson Imaging 1992;10:245–256.
124. Lipnick S, Verma G, Ramadan S, Furuyama J, Thomas MA. Echo planar correlated spectroscopic imaging: implementation and pilot evaluation in human calf in vivo. Magn Reson Med 2010;64:947–956.
125. Hoult DI, Lauterbur PC. Sensitivity of the zeugmatographic experiment involving human samples. J Magn Reson 1979;34: 425–433.
126. Barker PB, Hearshen DO, Boska MD. Single-voxel proton MRS of the human brain at 1.5T and 3.0T. Magn Reson Med 2001; 45:765–769.
127. Gonen O, Gruber S, Li BS, Mlynarik V, Moser E. Multivoxel 3D proton spectroscopy in the brain at 1.5 versus 3.0 T: signal-to-noise ratio and resolution comparison. AJNR Am J Neuroradiol 2001;22:1727–1731.
128. Kantarci K, Reynolds G, Petersen RC, et al. Proton MR spectroscopy in mild cognitive impairment and Alzheimer disease: comparison of 1.5 and 3 T. AJNR Am J Neuroradiol 2003;24: 843–849.
129. Ugurbil K, Adriany G, Andersen P, et al. Ultrahigh field magnetic resonance imaging and spectroscopy. Magn Reson Imaging 2003;21:1263–1281.
130. Hetherington HP, Pan JW, Chu WJ, Mason GF, Newcomer BR. Biological and clinical MRS at ultra-high field. NMR Biomed 1997;10:360–371.
131. Tkac I, Andersen P, Adriany G, Merkle H, Ugurbil K, Gruetter R. In vivo H-1 NMR spectroscopy of the human brain at 7 T. Magn Reson Med 2001;46:451–456.
132. Gruetter R, Weisdorf SA, Rajanayagan V, et al. Resolution improvements in in vivo 1H NMR spectra with increased magnetic field strength. J Magn Reson 1998;135:260–264.
133. Katscher U, Bornert P, Leussler C, van den Brink JS. Transmit SENSE. Magn Reson Med 2003;49:144–150.
134. Zhu Y. Parallel excitation with an array of transmit coils. Magn Reson Med 2004;51:775–784.
135. Sodickson DK, Manning WJ. Simultaneous acquisition of spatial harmonics (SMASH): fast imaging with radiofrequency coil arrays. Magn Reson Med 1997;38:591–603.
136. Pruessmann KP, Weiger M, Scheidegger MB, Boesiger P. SENSE: sensitivity encoding for fast MRI. Magn Reson Med 1999;42: 952–962.

137. Griswold MA, Jakob PM, Heidemann RM, et al. Generalized autocalibrating partially parallel acquisitions (GRAPPA). Magn Reson Med 2002;47:1202–1210.
138. Tsai SY, Otazo R, Posse S, et al. Accelerated proton echo planar spectroscopic imaging (PEPSI) using GRAPPA with a 32-channel phased-array coil. Magn Reson Med 2008;59:989–998.
139. Wiesinger F, Van de Moortele PF, Adriany G, De Zanche N, Ugurbil K, Pruessmann KP. Parallel imaging performance as a function of field strength–an experimental investigation using electrodynamic scaling. Magn Reson Med 2004;52:953–964.
140. Ohliger MA, Grant AK, Sodickson DK. Ultimate intrinsic signal-to-noise ratio for parallel MRI: electromagnetic field considerations. Magn Reson Med 2003;50:1018–1030.
141. Wiesinger F, Boesiger P, Pruessmann KP. Electrodynamics and ultimate SNR in parallel MR imaging. Magn Reson Med 2004; 52:376–390.
142. Lin F, Tsai SY, Lin YR, et al. Single-shot proton MR spectroscopic inverse imaging. In Proceedings of the 16th Annual Meeting of ISMRM, Toronto, Canada, 2008. (abstract 595).
143. Otazo R, Lin FH, Wiggins G, Jordan R, Sodickson D, Posse S. Superresolution parallel magnetic resonance imaging: application to functional and spectroscopic imaging. Neuroimage 2009; 47:220–230.
144. Lustig M, Donoho D, Pauly JM. Sparse MRI: the application of compressed sensing for rapid MR imaging. Magn Reson Med 2007;58:1182–1195.
145. Gruetter R, Adriany G, Choi IY, Henry PG, Lei H, Oz G. Localized in vivo 13C NMR spectroscopy of the brain. NMR Biomed 2003;16:313–338.
146. Ardenkjaer-Larsen JH, Fridlund B, Gram A, et al. Increase in signal-to-noise ratio of > 10,000 times in liquid-state NMR. Proc Natl Acad Sci U S A 2003;100:10158–10163.
147. Larson PE, Hu S, Lustig M, et al. Fast dynamic 3D MR spectroscopic imaging with compressed sensing and multiband excitation pulses for hyperpolarized 13C studies. Magn Reson Med 2011;65:610–619.